ETSI GR RIS 007 V1.1.1 (2026-02)

GROUP REPORT

Reconfigurable Intelligent Surfaces (RIS); Near-field Channel Modelling and Mechanics

Disclaimer

The present document has been produced and approved by the Reconfigurable Intelligent Surfaces (RIS) ETSI Industry Specification Group (ISG) and represents the views of those members who participated in this ISG.
It does not necessarily represent the views of the entire ETSI membership.

Reference
DGR/RIS-007

Keywords
channel model, near-field, RIS, technical solution

ETSI

650 Route des Lucioles
F-06921 Sophia Antipolis Cedex - FRANCE

Tel.: +33 4 92 94 42 00 Fax: +33 4 93 65 47 16

Siret N° 348 623 562 00017 - APE 7112B
Association à but non lucratif enregistrée à la
Sous-Préfecture de Grasse (06) N° w061004871

Contents

Intellectual Property Rights

Essential patents

IPRs essential or potentially essential to normative deliverables may have been declared to ETSI. The declarations pertaining to these essential IPRs, if any, are publicly available for **ETSI members and non-members**, and can be found in ETSI SR 000 314: *"Intellectual Property Rights (IPRs); Essential, or potentially Essential, IPRs notified to ETSI in respect of ETSI standards"*, which is available from the ETSI Secretariat. Latest updates are available on the ETSI IPR online database.

Pursuant to the ETSI Directives including the ETSI IPR Policy, no investigation regarding the essentiality of IPRs, including IPR searches, has been carried out by ETSI. No guarantee can be given as to the existence of other IPRs not referenced in ETSI SR 000 314 (or the updates on the ETSI Web server) which are, or may be, or may become, essential to the present document.

Trademarks

The present document may include trademarks and/or tradenames which are asserted and/or registered by their owners. ETSI claims no ownership of these except for any which are indicated as being the property of ETSI, and conveys no right to use or reproduce any trademark and/or tradename. Mention of those trademarks in the present document does not constitute an endorsement by ETSI of products, services or organizations associated with those trademarks.

DECT™, **PLUGTESTS™**, **UMTS™** and the ETSI logo are trademarks of ETSI registered for the benefit of its Members. **3GPP™**, **LTE™** and **5G™** logo are trademarks of ETSI registered for the benefit of its Members and of the 3GPP Organizational Partners. **oneM2M™** logo is a trademark of ETSI registered for the benefit of its Members and of the oneM2M Partners. **GSM®** and the GSM logo are trademarks registered and owned by the GSM Association.

Foreword

This Group Report (GR) has been produced by ETSI Industry Specification Group (ISG) Reconfigurable Intelligent Surfaces (RIS).

Modal verbs terminology

In the present document "**should**", "**should not**", "**may**", "**need not**", "**will**", "**will not**", "**can**" and "**cannot**" are to be interpreted as described in clause 3.2 of the ETSI Drafting Rules (Verbal forms for the expression of provisions).

"**must**" and "**must not**" are **NOT** allowed in ETSI deliverables except when used in direct citation.

1 Scope

The present document will identify Reconfigurable Intelligent Surfaces (RIS)-aided near-field communication system, including the use cases and scenarios for near-field RIS-aided system, the channel modelling for RIS-aided communications in the near-field region, new technical solutions/mechanisms applicable for RIS-aided system in the near field, and the potential specification impact.

2 References

2.1 Normative references

Normative references are not applicable in the present document.

2.2 Informative references

References are either specific (identified by date of publication and/or edition number or version number) or non-specific. For specific references, only the cited version applies. For non-specific references, the latest version of the referenced document (including any amendments) applies.

NOTE: While any hyperlinks included in this clause were valid at the time of publication, ETSI cannot guarantee their long-term validity.

The following referenced documents may be useful in implementing an ETSI deliverable or add to the reader's understanding, but are not required for conformance to the present document.

[i.1] ETSI GR RIS 001: "Reconfigurable Intelligent Surfaces (RIS); Use Cases, Deployment Scenarios and Requirements".

[i.2] ETSI GR RIS 002: "Reconfigurable Intelligent Surfaces (RIS); Technological challenges, architecture and impact on standardization".

[i.3] ETSI GR RIS 003: "Reconfigurable Intelligent Surfaces (RIS); Communication Models, Channel Models, Channel Estimation and Evaluation Methodology".

[i.4] IEC/EN 62311:2020: "Assessment of electronic and electrical equipment related to human exposure restrictions for electromagnetic fields (0 Hz - 300 GHz)".

[i.5] W. C. Chew: "Waves and Fields in Inhomogenous Media", Hoboken, NJ, USA, Wiley, 1995.

[i.6] H. Jiang et al.: "A general wideband non-stationary stochastic channel model for intelligent reflecting surface-assisted MIMO communications", IEEE Trans. Wireless Commun., vol. 20, no. 8, pp. 5314-5328, August 2021.

[i.7] R. Liu, J. Dou, P. Li, J. Wu and Y. Cui: "Simulation and Field Trial Results of Reconfigurable Intelligent Surfaces in 5G Networks", in IEEE™ Access, vol. 10, pp. 122786-122795, 2022.

[i.8] H. Jiang et al.: "Large-Scale RIS Enabled Air-Ground Channels: Near-Field modelling and Analysis", in IEEE™ Transactions on Wireless Communications.

[i.9] RP-234018 New SID: "Study on channel modelling enhancements for 7-24GHz for NR".

[i.10] V.Arun, H.Balakrishnan: "Rfocus: beamforming using thousands of passive antennas", Proc. 17th USENIX Symposium on Networked Systems Design and Implementation (NSDI)?(2020), pp. 1047-1061, doi: 10.1109/TVT.2023.3311868.

[i.11] B. Zhu, et al.: "Switchable metamaterial reflector/absorber for different polarized electromagnetic waves", Appl. Phys. Lett. 97 (051906).

[i.12] C. Wu, et al.: "Two-Stage Hierarchical Beam Training for Near-Field Communications", in IEEE™ Transactions on Vehicular Technology, vol. 73, no. 2, pp. 2032-2044, February 2024, doi: 10.1109/TVT.2023.3311868.

[i.13] X. Mu, J. Xu, Y. Liu and L. Hanzo: "Reconfigurable Intelligent Surface-Aided Near-Field Communications for 6G: Opportunities and Challenges", in IEEE™ Vehicular Technology Magazine, vol. 19, no. 1, pp. 65-74, March 2024.

[i.14] X. Wei, L. Dai, Y. Zhao, G. Yu and X. Duan: "Codebook design and beam training for extremely large-scale RIS: Far-field or near-field?", in China Communications, vol. 19, no. 6, pp. 193-204, June 2022.

[i.15] C. Liu et al.: "A Radiation Viewpoint of Reconfigurable Reflectarray Elements: Performance Limit, Evaluation Criterion, and Design Process", in IEEE™ Transactions on Antennas and Propagation, vol. 71, no. 10, pp. 7881-7891, October 2023, doi: 10.1109/TAP.2023.3301609.

[i.16] Q. Wu, S. Zhang, B. Zheng, C. You, and R. Zhang: "Intelligent reflecting surface-aided wireless communications: A tutorial", IEEE™ Trans. Commun., vol. 69, no. 5, pp. 3313-3351, 2021.

[i.17] G. Chen et al.: "Intelligent reflecting surface aided MIMO networks: Distributed or centralized architecture?", IEEE™ Trans. Wireless Commun., vol. 23, no. 12, pp. 18969-18986, December 2024.

[i.18] ETSI GR RIS 006: "Multi-functional Reconfigurable Intelligent Surfaces (RIS): Modelling, Optimization, and Operation".

[i.19] Y Zhu, Q Wu, W Chen, Y Liu, and R Liu: "A flexible design for beam squint effect suppression in IRS-aided THz communications", arXiv preprint arXiv:2508.21295, 2025.

[i.20] X. Cao, M. Mohammadi, H. Q. Ngo, and M. Matthaiou: "RIS-assisted XL-MIMO for coexistence of near-field and far-field communications", in Proc. IEEE™ WCNC, April 2024, pp. 1-6.

[i.21] X. Liu, Q. Wu, D. Hu, R. Wang and J. Wu: "Hierarchical Codebook Design and Analytical Beamforming Solution for IRS-Assisted Communication", in IEEE™ Transactions on Wireless Communications, vol. 23, no. 8, pp. 8924-8938, August 2024.

[i.22] A. T. Joy, A. Tishchenko, H. Taghvaee, P. Mursia, V. Sciancalepore and M. Khalily: "RIS-Enabled ISAC in 6G: Exploring the Role of Wave Domain Computing", in IEEE™ Communications Standards Magazine, 2025.

[i.23] Y. Hou, G. Wang, C. Chen, G. Mu, Q. Cui, X. Tao, and Y. Yang: "220 GHz RIS-aided multi-user terahertz communication system: Prototype design and over-the-air experimental trials", arXiv preprint arXiv:2502.16970, 2025.

[i.24] R. Liu et al.: "Integrated sensing and communication based outdoor multi-target detection, tracking, and localization in practical 5G Networks", in Intelligent and Converged Networks, vol. 4, no. 3, pp. 261-272, September 2023.

[i.25] H. Lu and Y. Zeng: "Communicating With Extremely Large-Scale Array/Surface: Unified modelling and Performance Analysis", in IEEE™ Transactions on Wireless Communications, vol. 21, no. 6, pp. 4039-4053, June 2022.

[i.26] Y. Jiang, F. Gao, M. Jian, S. Zhang and W. Zhang: "Reconfigurable Intelligent Surface for Near Field Communications: Beamforming and Sensing", in IEEE™ Transactions on Wireless Communications, vol. 22, no. 5, pp. 3447-3459, May 2023.

[i.27] N. M. Estakhri and A. Alú: "Wave-front transformation with gradient metasurfaces", Phys. Rev. X, vol. 6, no. 4, October 2016.

[i.28] W. Hao, L. Yang, G. Sun, Q. Wu, and C. Huang: "Robust beamforming optimization for RIS-assisted THz ISAC systems", IEEE™ Trans. Veh. Technol., vol. 74, no. 11, pp. 17754-17764, November 2025.

[i.29] Q. Zhu, T. Tang, J. Wang, D. Kong, P. Liu and R. Liu: "Separate Channel Estimation for RIS-Assisted Orbital Angular Momentum Communication Systems", in IEEE™ Transactions on Green Communications and Networking, 2026.

3 Definition of terms, symbols and abbreviations

3.1 Terms

For the purposes of the present document, the terms given in ETSI GR RIS 001 [i.1], ETSI GR RIS 002 [i.2] and ETSI GR RIS 003 [i.3] apply.

3.2 Symbols

Void.

3.3 Abbreviations

For the purposes of the present document, the following abbreviations apply:

BS	Base Station
CSI	Channel State Information
LoS	Line Of Sight
MIMO	Multiple Inputs Multiple Outputs
NLOS	None Line Of Sight
OAM	Orbital Angular Momentum
RIS	Reconfigurable Intelligent Surface
SIMO	Single Inputs Multiple Outputs
SNR	Signal to Noise Ratio
UE	User Equipment
ULA	Uniform Linear Array

4 Characterization of near-field propagation

4.1 General Introduction

MIMO technology (e.g. Extremely Large Antenna Array (ELAA), Distributed-MIMO (D-MIMO)) is an essential aspect to enable the next communication system. With the increasing of the effective antenna aperture, a paradigm shift for the channel characteristics can be clearly observed, i.e. from far-field propagation to near-field propagation. The details of far-field and near-field propagation characteristics are described below:

- For the far-field propagation, the plane wavefront is assumed for the propagation of electromagnetic waves as approximation. Then, the parameter of each path received/transmitted from different antenna elements, e.g. angle (e.g. AOA, AOD) are assumed to be same.
- For the near-field propagation, the wavefront of electromagnetic waves in the near-field region can be approximated as spherical wave and the angle of links between each antenna element of Tx and Rx are different, resulting in a non-linear parameters variation.
- The calculation of electromagnetic field in the far-field and the near-field regions of an antenna is considered in Annex A of IEC/EN 62311:2020 [i.4] and can be derived one from the other.

Considering such characteristics of near-field propagation, the existing communication algorithms based on the far-field propagation may suffer serious performance losses in the near-field scenarios, or cannot take full advantage of such new features to achieve the best performance. Although RIS technology has been demonstrated to perform well in far-field region [i.7], work on near-field needs to be done. In such, this clause firstly illustrate the definition of the near field electromagnetic effect from the theoretical analysis aspect, then give the preliminary simulation and performance results to further observe and evaluate the characterization of near-field propagation.

4.2 Theoretical analysis

4.2.1 Typical near-field scenarios

For a MIMO scenario with K single antenna users at the transmitter and N antennas at the receiver, the signal sent by the k-th user to the n-th antenna can be written by Green's function [i.5]:

$$y_{k,n} = \frac{1}{4\pi \| \boldsymbol{p}_k - \boldsymbol{p}_n \|} e^{-j\frac{2\pi}{\lambda}\| \boldsymbol{p}_k - \boldsymbol{p}_n \|} + n_\sigma,$$

where λ is the wavelength of the signal, p_k and p_n are the position coordinates of the user and the n-th antenna, respectively. Whether the user is in the far field or near field depends on the value of $\frac{2\pi}{\lambda}\| p_k - p_n \|$. According to the causes of the near field, the near field can be divided into the following three cases.

Near-field of short distance communication: The reason for the near-field phenomenon is that $||p_k||$ is relatively small. In this case, the distance between the user and the array is relatively short, resulting in a large curvature of the wavefront, so the curvature cannot be ignored as 0. Therefore, spherical wave and near-field model are needed. This case often occurs in the indoor communication scene, where the scattering environment is rich and the multipath effect is obvious. However, due to the slow movement of indoor users, the Doppler effect is not obvious. The main difficulty of beamforming design and user location estimation in this case is the processing of multi-paths.

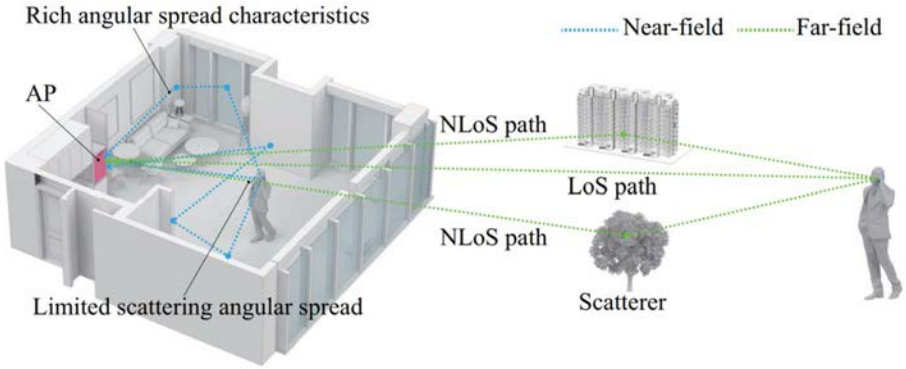

Figure 4.2.1-1: Near-field of short distance communication

Near-field of large size array: The reason for the near-field phenomenon is that $||p_N - p_0||$ is large, where p_0 is the coordinate of the reference antenna. In this case, even if the curvature of the incoming wave is small, since the radian of the wave front is large, the plane wave far-field model cannot be used for modelling. In this case, the main difficulty of beamforming design is the estimation of the curvature of the incoming wave.

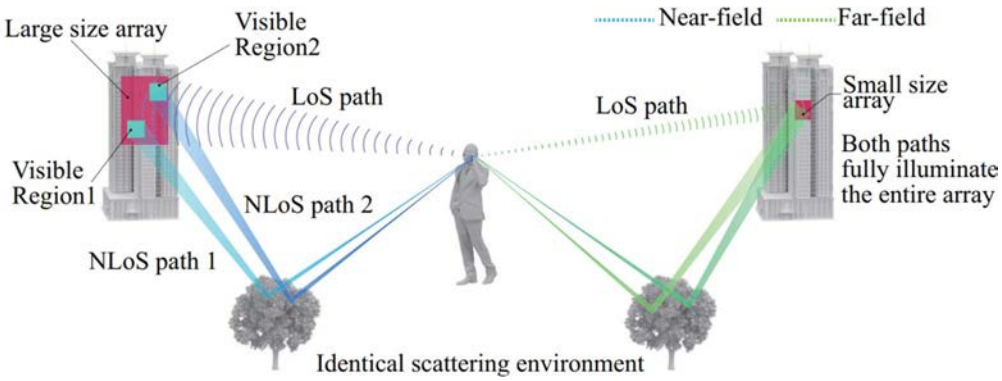

Figure 4.2.1-2: Near-field of large size array

Near-field of high frequency: The reason for the near-field phenomenon is that λ is small. In this case, electromagnetic waves have high spatial resolution, so even if the radian and curvature of the wavefront are relatively small, the plane wave model cannot be used. Due to the sparse nature of high-frequency channels, the location algorithms usually need to be done where there are few anchor points. In addition, due to the high spatial resolution of high-frequency beams, higher accuracy is required for channel parameters estimation and user location estimation process.

It should be pointed out that since $||p_k||$, $||p_N - p_0||$, and λ are three independent variables, these three cases are not mutually exclusive. Therefore, it need to study the changes that these three cases will bring to beamforming design, etc.

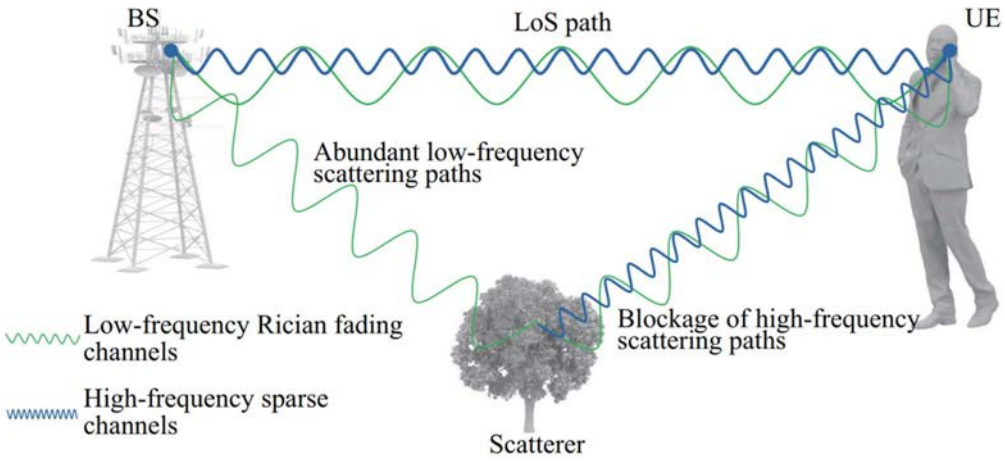

Figure 4.2.1-3: Near-field of high frequency

The three scenarios mentioned above represent typical near-field cases. In practical applications, combinations of these scenarios or non-canonical near-field situations may occur. Two illustrative examples are provided.

EXAMPLE 1: When employing high-frequency signals for communication in densely built environments, RIS can provide virtual line-of-sight links. However, since high-frequency signals suffer severe channel attenuation, ultra-large-scale arrays are often required to deliver sufficient beamforming gain. This scenario simultaneously belongs to both the ultra-large-scale array near-field and high-frequency near-field categories.

EXAMPLE 2: When using RIS for blind zone coverage in underground garages, multiple RIS units are typically deployed on garage walls to significantly enhance signals. Given the indoor characteristics of garages, the short distance between RIS and users makes this scenario concurrently exhibit both short-range near-field and ultra-large-scale array near-field properties.

Therefore, in practical applications, researchers should avoid vaguely claiming a "near-field scenario" without specification. Instead, rigorous analysis can identify the exact causes of near-field effects in each specific case, then select appropriate research methodologies for algorithm design accordingly.

It should be emphasized that although all three scenarios may occur in practical applications, the main motivation for near-field research at present is to serve high-frequency communication. In high-frequency scenarios, due to the increase in Rayleigh distance, a large number of users are in the near-field area, making near-field communication a research focus.

4.2.2 Comparative Analysis of Angular vs. Depth Beam Squint in THz Near-Field RIS

The transition to TeraHertz (THz) communications necessitates the use of extremely large-scale RIS arrays to compensate for propagation loss. This increase in aperture size (D) combined with high frequency (λ) dramatically extends the Rayleigh distance ($R=2D^2/\lambda$), making the radiative near-field the dominant operational region for typical indoor and hotspot scenarios. In this context, the beam squint effect induced by wideband signals manifests in two dimensions: angular squint (transverse deviation) and focal depth squint (longitudinal deviation). While angular squint is well-known in far-field models, our analysis reveals that in the near-field, the dispersion along the distance axis is significantly more severe and detrimental.

To quantify and compare these two effects, a typical THz RIS scenario has been analysed. Consider a system operating at a center frequency f_c=300 GHz with a Base Station-to-RIS distance d^{BR}=80 m. A user is located in the near-field at a distance d^{RU}=5 m from the RIS, at a steering angle of $\theta_0=45^\circ$. The beam deviation for an edge subcarrier at f_m=315 GHz (5 % bandwidth deviation) has been examined. First, it calculates the angular squint (lateral deviation). Based on standard phased array theory, the squinter beam angle θ' is related to $\sin(\theta')=(f_c/f_m)\sin(\theta_0)$. For $f_m=1{,}05f_c$, the angle shifts from 45° to approximately 42,3 degrees ($\Delta\theta\approx2{,}7^\circ$). At a distance of 5 m, this results in a lateral spatial offset of approximately $\Delta L\approx5\times\sin(2{,}7^\circ)\approx0{,}24$ m.

Second, it calculates the focal depth squint (longitudinal deviation). Using our derived near-field dispersion relationship:

$$d^{RU'}\approx\frac{2(d^{BR}+d^{RU})}{1+f_m/f_c}-d^{BR}$$

Substituting the values (d^{BR}=80,d^{RU}=5,f_m/f_c=1,05), the actual focal point shifts to$d^{RU'}\approx$2,93 m. This results in a longitudinal spatial offset of $\Delta D=|5-2{,}93|\approx2{,}07$ m.

The quantitative comparison reveals that the error in the distance dimension (2,07 m) is nearly an order of magnitude larger than the error in the angular dimension (0,24 m). As the user is located deeply within the near-field, this longitudinal defocusing causes the signal energy to spread along the propagation path rather than concentrating at the UE, leading to a catastrophic loss of array gain. Conventional channel models that only account for angular deviation underestimate this impairment, which leads to significant performance degradation for wideband signals. In conclusion, this contribution identifies near-field focal depth dispersion as the primary physical impairment for wideband THz RIS. The analysis demonstrates that accurate channel modelling for such systems necessitates incorporating distance-dependent dispersion characteristics beyond conventional angular-only parameters.

4.2.3 Revisiting Power Scaling Laws for High-Frequency Near-Field RIS: From Quadratic Growth to Arctangent Saturation

In High-Frequency (mmWave and THz) RIS systems, the pursuit of sufficient link budget necessitates physically extensive apertures where the physical dimension L is much larger than the wavelength λ, inevitably pushing the system into the radiative near-field. In this regime, the conventional far-field assumption that received power scales quadratically with the number of elements ($P_{RX}\propto N^2\propto A_{phys}^2$) becomes inapplicable because it is predicated on the Uniform Plane Wave (UPW) approximation which assumes a constant channel gain across all elements. While valid for compact arrays, this assumption is insufficient for physically large surfaces where signal amplitude variations are significant. By applying the Unified Field Integration Model derived in [i.25], it demonstrates that the actual power scaling follows a Squared Arctangent Law, governed by the projected solid angle rather than the discrete element count.

Specifically, for a planar RIS of size $L_y \times L_z$ deployed at a perpendicular distance D_0 from the transmitter or receiver, the effective accumulated channel gain is not a linear sum of N, but is determined by the integral of the projected aperture over the surface. Based on the closed-form derivation in Theorem 1 of [i.25], the effective array gain factor G_{eff} for a near-field surface is quantified as a summation of arctangent functions:

$$G_{eff}(L_y, L_z) = \frac{\xi}{4\pi} \sum_{k=1}^{4} \arctan\left(\frac{Y_k Z_k}{D_0 \sqrt{D_0^2 + Y_k^2 + Z_k^2}} \right)$$

In this expression, ξ denotes the array occupation ratio representing the effective reflecting element area relative to the unit cell area, while Y_k and Z_k represent the geometric integration boundaries defined by the relative coordinates of the RIS corners with respect to the user's projection point. Physically, the arctangent term calculates the Solid Angle subtended by the RIS at the user's location. Consequently, the received signal power for the RIS-assisted link follows the square of this geometric accumulation:

$$P_{RX}^{RIS} \propto \left| G_{eff}^{TX \to RIS} \cdot G_{eff}^{RIS \to RX} \right| \propto \left| \arctan\left(\frac{L_y L_z}{4 D_0^2} \right) \right|^2$$

This quantitative model reveals two distinct scaling regimes based on the physical size of the RIS relative to the projection distance. In the small size or far-field regime where $L \ll D_0$, the linear approximation $\arctan(x) \approx x$ holds, meaning the gain factor becomes proportional to the area $L_y L_z$. Since the number of elements N is proportional to the area, the power scales as N^2, recovering the conventional far-field quadratic scaling law. However, in the large size or near-field regime where $L \gg D_0$, the arctangent function saturates to $\pi/2$. In this case, the received power decouples from N and converges to a constant saturation limit approximately equal to $P_{TX} \cdot (\xi/2)^2$. This analysis rigorously proves that simply expanding the RIS physical area yields diminishing returns in the near-field region, necessitating a shift in design optimization from maximizing surface area to maximizing the effective angular span.

4.3 Performance analysis

4.3.1 Observation on the near-field effect

Within the evolution from 5G large-scale array communication to future ultra-large-scale array communication, not only the number of antennas array size will be significantly increased, the channel characteristics will also have fundamentally changes.

As described in clause 4.11, the plane wavefront propagation of electromagnetic waves is assumed for the far-field propagation, then the parameter of each path received/transmitted from different antenna elements are assumed to be same, while the parameters for each links between each antenna element of Tx and Rx are different for the near-field propagation. To clearly observe such features of near-field propagation, the realistic measurement work has been carried out in an indoor scenario as shown in Figure 4.3.1-1.

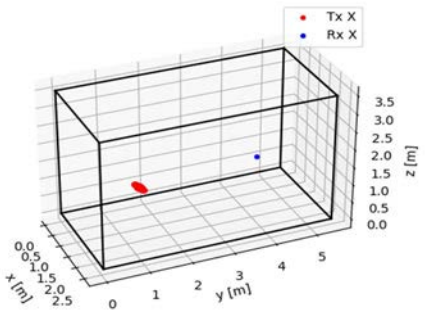

Figure 4.3.1-1: Measurement scenarios

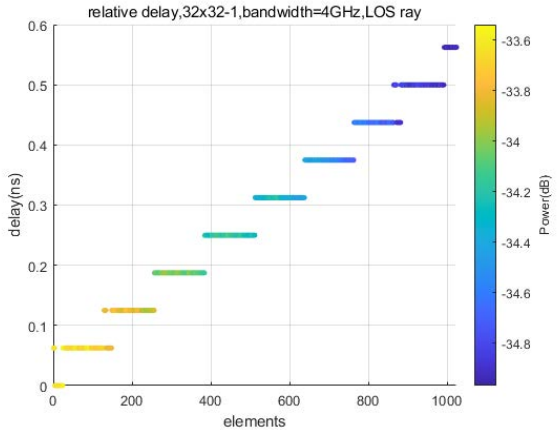

Figure 4.3.1-2: Delay and power measurement results among different antenna elements

From the measurement results shown in Figure 4.3.1-2, with the large aperture size configuration on the Tx side, the parameter variation among different antenna elements of Rx can be observed, which clearly shows and verifies that the near-field propagation effect has the different propagation characteristics from the far-field propagation.

4.3.2 Performance analysis

In clause 4.3.1, the near-field effect can be clearly observed according to the measurement results. In this clause, analysis on the performance of near-field propagation can be also provided.

In order to evaluate the performance of near-field channel model, the simulation has been done following the near-field channel model methodology for LoS channel according to the latest agreements on 3GPP R19 FR3 channel model. As shown in following Figure 4.3.2-1, with considering the impact of the near-field, the improvement on both rank and throughput can be achieved compared with the far-field channel. In this way, the research on the near-field channel model and the corresponding technical solutions is essential.

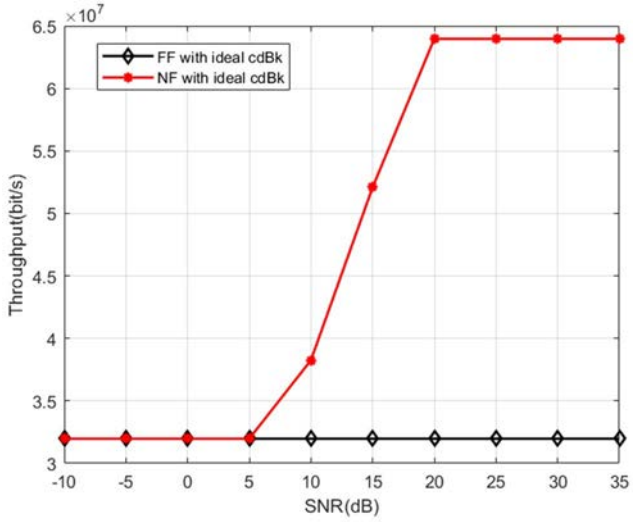

(a) Throughput performance

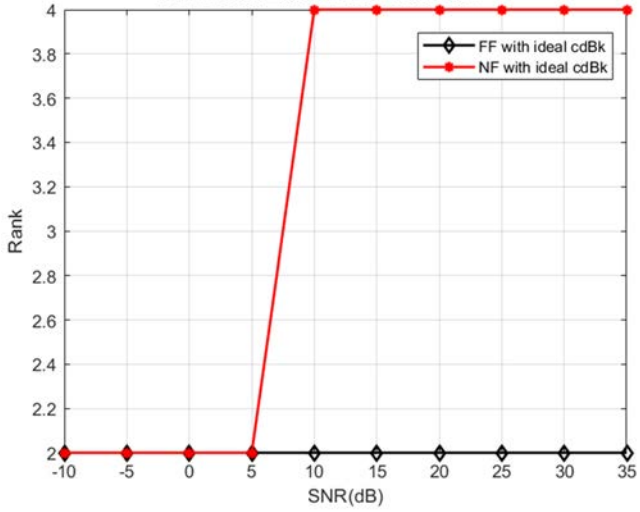

(b) Rank performance

NOTE: The simulation results can be applicable for the channel between two points, and any of two points can be relevant to RIS.

Figure 4.3.2-1: Rank and throughput performance

4.4 Characterizing RIS Near-Field by Simulation and Measurement

Apart from theoretical analysis, simulations or measurements can also be used as a valid approach to characterize near-field effect in RIS-aided communication systems. Near-field measurement provides a reliable method for directly characterizing and verifying performance within a new "near-field paradigm". Within this region, electromagnetic waves are spherical, with non-linear spatial variations in both phase and amplitude. Far-field measurement methods become unsuitable here and can even yield entirely incorrect conclusions. How the data obtained from near-field measurements to understand and optimize the performance of RIS in near-field communication is a highly significant research topic.

The most commonly used method for near-field simulation or measurement is planar near-field scanning. Its operating principle involves a probe measuring the tangential electromagnetic field components, Ex and Ey, or signals related to them, generated by the RIS in the near-field region. To accurately reconstruct the field distribution, the sampling interval should satisfy the Nyquist criterion, typically requiring Δx, $\Delta y < \lambda/2$. Otherwise, aliasing errors will occur. Assuming the measured tangential electric field on the plane z=0 is E_t(x, y, 0), a two-dimensional Fourier transform is performed to obtain the amplitude and phase of the corresponding plane waves in the spatial frequency domain:

$$F(k_x,\ k_y) = \iint_{-\infty}^{\infty} E_t\ (x,\ y,\ 0)\ e^{j\ (k_x x + k_y y)}\ dxdy.$$

In the equation, Et(x, y, 0) represents the measured distribution of the near-field tangential electric field, and F(k_x, k_y) denotes the complex amplitude of the plane wave components propagating in different directions, where k_x, k_y are related to the spatial frequencies. This process effectively decomposes the spatially varying near-field signal into countless plane waves, each characterized by its specific propagation direction (k_x, k_y). When operating at high frequencies such as terahertz, strong electromagnetic coupling arises between the densely packed elements of the RIS, and surface waves may be excited. These effects can severely distort the intended wavefront, leading to degraded focusing performance. Near-field measurement stands as the singular method capable of directly visualizing and quantifying these non-ideal effects. It enables the direct measurement of the actual phase distribution generated by the RIS surface.

During simulation or measurement, a finite number of sample points will be taken and used. The number of samples can be chosen so that the results obtained are smooth enough. The general measurement setup can be illustrated using Figure 4.4-1. As an example, a 16×8 RIS operating on 210 GHz is considered. Figure 4.4-1 depicts the array surface positions corresponding to the RIS sampling positions and Figure 4.4-2 shows the amplitudes obtained for the reflected signals from the RIS. As to phase correction, received data is first transformed from the spatial domain to the frequency domain. The zero-frequency component of the frequency-domain data is shifted to the center of the spectrum. Filtering is applied within the frequency domain. Finally, the data is shifted back to its original position before undergoing a two-dimensional inverse fast Fourier transform. This procedure facilitates effective phase correction, yielding readily interpretable data crucial for optimizing near-field communication systems. Figure 4.4-3 shows the phase distribution on RIS. By comparing this measured phase distribution with the theoretical design, the accuracy and dynamic range of the phase manipulation capabilities can be characterized, forming the basis for phase calibration.

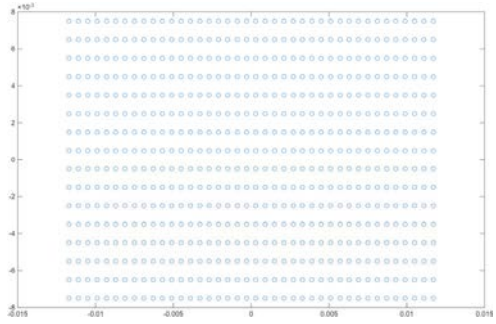

Figure 4.4-1: Sampling positions on a 16×8 RIS on 210 GHz

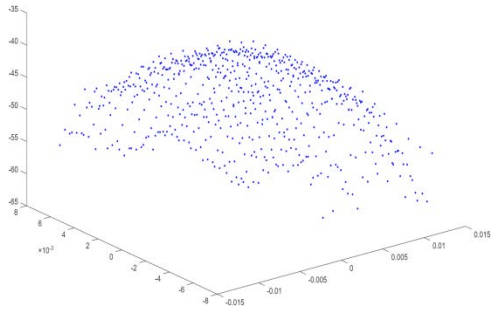

Figure 4.4-2: Amplitudes of reflected signals on the 16×8 RIS

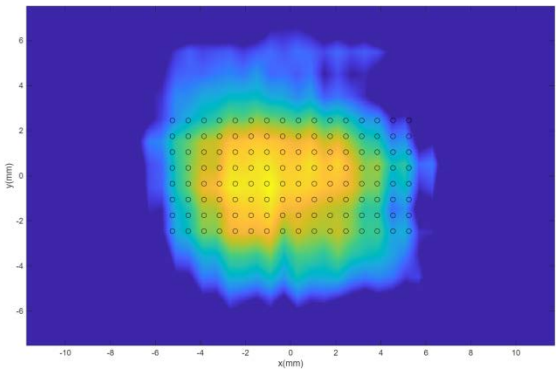

Figure 4.4-3: Phase distribution of reflected signals on the 16×8 RIS

5 Description of scenarios and use cases for RIS-aided near-field system

5.1 General introduction

As introduced in ETSI GR RIS 002 [i.2] and ETSI GR RIS 003 [i.3], RIS is consisted of a large number of low-cost reconfigurable units, which can be considered as one of key technologies in the future 6G communication systems. Deploying RIS refers to a new type of system node with reconfigurable surface technology, where its response can be adapted to the status of the propagation environment through control signaling, thereby improving communication quality and coverage range. While considering the RIS with larger array and higher operating frequency, the near-field region of RIS assisted communication links should be considered and cannot be ignored. It is therefore important to develop a clear understanding of the deployment scenarios and use cases of RIS-aided near-field system, which is beneficial for the further channel model and technical solution study.

5.2 Deployment scenarios of RIS-aided near-field system

5.2.0 General

In ETSI GR RIS 001 [i.1], there has already some deployment scenarios described, including the outdoor, indoor and hybrid scenarios. While considering the RIS-aided near-field system, the potential near-field region in the deployment scenarios should be further considered as following.

5.2.1 Outdoor scenarios

For the Outdoor scenarios, the RIS can be configured with large array and higher frequencies, allowing the near-field region to extend beyond the minimum distance typically delineated between Base Stations (BS) and User Equipment (UE). For example, for the downlink, this scenario may result in receivers being situated within the near-field region, while the transmitter may be located in the near-field region for the uplink. And compared with far-field propagation region, the near-field propagation channels can have better and higher rank conditions due to the non-linear channel parameters. Consequently, deploying RISs in outdoor scenarios leverages these near-field attributes to support multiple orthogonal links simultaneously, then the higher throughput and space division multiple access can be achieved.

Considering that the RIS with larger aperture size of array, one potential way is to deploy the RIS on the surfaces of buildings, such as the RIS being attached to the surfaces of some buildings, to provide the better services for the outdoors UEs located in the near-field region of RIS. For example as following Figure 5.2.1-1, the centralized RIS with larger aperture size is deployed on the surface of a high building, and by designing the specific codebook that utilizing the near-field propagation characteristics for the centralized RIS, the co-channel interference of two served outdoor UEs at a same direction can be reduced. In this case, by deploying the RIS with larger aperture size, there is no need to use the large antenna array to realize the higher throughout.

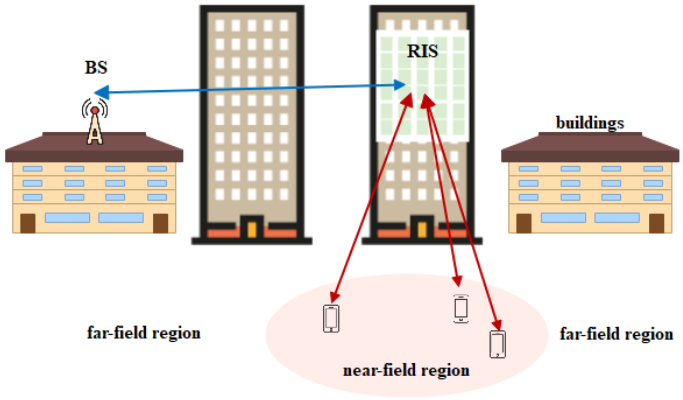

Figure 5.2.1-1: Example of Outdoor scenarios to deploy centralized RIS in the downlink

5.3 Potential use cases of RIS-aided near-field system

5.3.1 Passive RIS-aided near field positioning

One of the typical applications of the RIS technology is to obtain sufficient beamforming gain through hundreds or even thousands of reflective elements for coverage. The larger array size and higher operating frequency further expand the near-field area for RIS-aided communication systems. In the far-field region, the rank of the channel can sometimes be small, which restricts the spatial multiplexing gain of the channel [i.6]. On the other hand, due to the nonlinear changes in signal amplitude and phase caused by spherical waves, near-field channels have better rank conditions, which can effectively improve the multiplexing gain and useful spatial degrees of freedom of the system. When users are located in the radiative near-field region, even if multiple users have the same radiation angle, different near-field polar-domain codebooks can be configured on RIS to reduce co-channel interference through beam focusing, if the distances between each users and the BS are different [i.8]. Similarly, the degrees of freedom provided by the spherical wavefront and the near-field radiation wave carrying both angle and distance information further enhances the accuracy of wireless positioning and sensing.

To achieve positioning in RIS-aided near field, many algorithms require multidimensional spatial spectrum search or high-complexity computations, which restricts the practical application due to hardware limitations. Therefore, it is desirable to transform the multi-dimensional spectral peak search algorithm into several one-dimensional searches.

5.3.2 RIS-aided terahertz communications

TeraHertz (THz) communication has emerged as a promising technology for next-generation wireless networks. Thanks to its unique feature of large bandwidth, THz communication is suitable for many kinds of applications, such as high-speed data transfer, imaging, security scanning and so on. With the demand for faster communication development, THz communication is envisioned to play a crucial role in promoting enhanced Mobile Broadband (eMBB), enabling Ultra-Reliable Low-Latency Communications (URLLC), and facilitating the Internet-of-Things (IoT) networks. However, due to severe path loss and atmospheric absorption, the potential of THz communication is bottlenecked in practice. In the existing literature, the RIS has been demonstrated that it can significantly improve coverage, capacity, energy efficiency, and so on, via adjusting the phase of reflected signals for creating favourable communication channels. Hence, the RIS has been envisioned as a promising solution to the inherent shortcomings of THz communication systems, which has been verified by various researches.

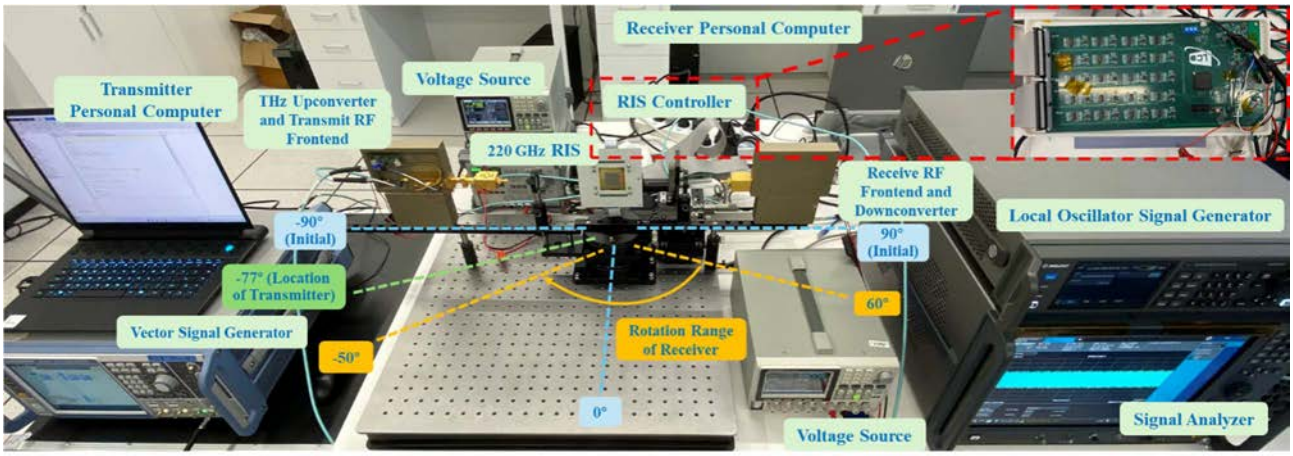

(a) The prototype of 220 GHz RIS-aided system

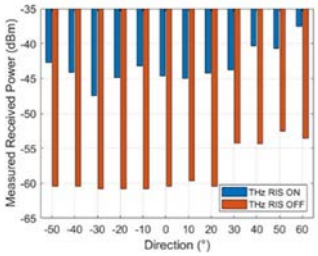

(b) Measured received power in the single-user scenario

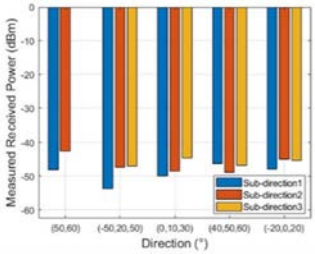

(c) Measured received power in the multi-user scenario

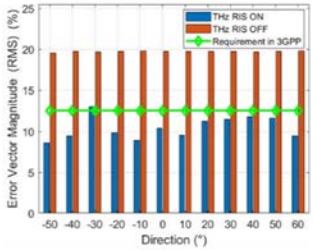

(d) Measured EVM of the received signal in the single-user scenario

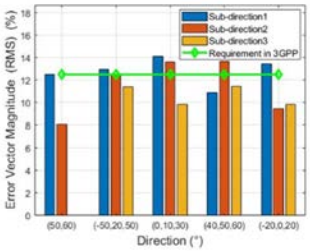

(e) Measured EVM of the received signal in the multi-user scenario

Figure 5.3.2-1

To demonstrate the benefit of RIS to THz communications, a prototype of a RIS-aided THz system operating at 220 GHz has been present, as shown in Figure 5.3.2-1(a), which can be performed over longer distances by increasing antenna or array gain while keeping the power amplifier within its linear region. The liquid-crystal RIS, which contains 80 strip-shaped units and enables highly directional THz beams in desired directions under a controlled voltage pattern, exhibits a reflection efficiency ranging from 3 % to 16 %. Other parameters are the same as those in Tables II and III of [i.23] and a Stochastic Parallel Gradient Descent (SPGD) optimization algorithm is adopted for Channel State Information (CSI) acquisition. The complete system consists of five main modules: baseband transmitter, THz upconversion mixer and transmit Radio Frequency (RF) front-end, RIS, receive RF front-end and THz downconversion mixer, and baseband receiver. The transmitter and receiver are mounted on two rotatable rails, respectively, while the RIS is fixed on the center of the rotation axis. The angular positions shown in Figure 5.3.2-1(a) correspond to the initial setup. During the experiment, the transmission link is blocked when the transmitter is positioned at -90°. Experimental results indicate that -77° is an appropriate deployment angle for the transmitter. Meanwhile, the receiver can rotate freely between -50° and 90°. In the single-user scenario, the RIS's beam pattern has been optimized for 12 directions from -50° to 60° in 10° intervals. In the multi-user scenario, the RIS's sub-beams have been optimized for five groups of sub-directions including two- and three-user setups:

- (50°, 60°);
- (-50°, 20°, 50°);
- (0°, 10°, 30°);
- (40°, 50°, 60°); and
- (-20°, 0°, 20°);

with each angle indicating one user direction.

Figure 5.3.2-1(b) shows the measured received power in a single-user scenario across angular directions from -50° to 60°. Compared to the case with the RIS deactivated, the activated RIS provides at least a 15 dB enhancement in received power across all directions. Interestingly, at larger angles such as 40°, 50° and 60°, relatively higher power levels are observed even without RIS activation. This is attributed to these directions being closer to the specular reflection angle, where sidelobe leakage from the incident signal contributes to increased power. Figure 5.3.2-1(c) presents the received power in a multi-user scenario for different sub-beam groups. Compared to the no-RIS case in Figure 5.3.2-1(b), each sub-beam demonstrates a substantial power gain, highlighting the RIS's capability in effectively forming directional beams to serve multiple users simultaneously. Figure 5.3.2-1(d) illustrates the measured Error Vector Magnitude (EVM) of the received signal across various directions in a single-user scenario, alongside the 3GPP-specified EVM threshold for reliable 16QAM demodulation. When the RIS is deactivated, EVM values in most directions exceed the threshold, indicating poor signal quality and unreliable demodulation. In contrast, activating the RIS significantly reduces the EVM in most directions, bringing them below the threshold and thereby enabling accurate demodulation with lower bit error rates. Figure 5.3.2-1(e) shows the EVM performance for different sub-beam groups in a multi-user scenario. Compared to the single-user case in Figure 5.3.2-1(d), a slight degradation is observed, and certain sub-directions fail to meet the demodulation threshold-suggesting the presence of bit errors. This can be mitigated by deploying a larger RIS aperture in practice. Nevertheless, compared to the RIS-off case, most sub-beams still achieve considerable EVM improvement.

These experimental results validate that integrating RIS into THz communication systems significantly enhances link quality, broadens angular coverage, and supports efficient multi-user transmission.

6 Channel model of RIS-aided near-field system

6.1 General introduction

In clause 6, relevant scenarios, antenna configurations as well as detailed near-field channel models are introduced.

6.2 Scenarios and antenna configuration

6.2.1 Modelling RIS elements

Traditional channel models typically account for path loss, multipath effects and shadow fading. However, the introduction of RIS may introduce new factors, such as the reflective properties of RIS and the effects of mutual coupling between components. Therefore, the channel model needs to take these new factors into account. Particularly, near-field channel modelling is more complex, which requires more refined models and parameter estimation methods. At the same time, it also provides new degrees of freedom for optimization, and the performance of near-field communication can be improved through RIS. Therefore, an accurate RIS model for high frequency bands (including sub-THz and THz bands) will be beneficial for the near-field channel modelling. As a start, each RIS element can be modelled individually and its contribution to the channel is characterized by its reflection coefficients (amplitude and phase).

A schematic of an RIS element with a single switch is shown in Figure 6.2.1-1(a). RIS elements can usually be divided into two parts: switch and passive antenna structures, in which the incident wave comes from Floquet port and is scattered by the cell to produce reflected and transmitted waves, while part of the energy is absorbed by the cell and the switch. It is assumed that the majority of energy is reflected with no cross polarization [i.11]. It is worth noting that there is a reflective ground plane, meaning that no energy is transmitted, and the switch and substrate absorb minor energy. The element is surrounded by a periodic boundary. The different states of the switch can generate reflection coefficients with varying amplitude and phase. Assuming that the size of the lumped switch is significantly smaller than the operating wavelength λ, a lumped port can be defined at the switch location. Consequently, the passive element structure can be modeled as a two-port [S] parameter. Port 1 is connected to the free space, and port 2 is connected to the switch. The loaded switch is modeled as a variable impedance Z, as shown in Figure 6.2.1-1(b).

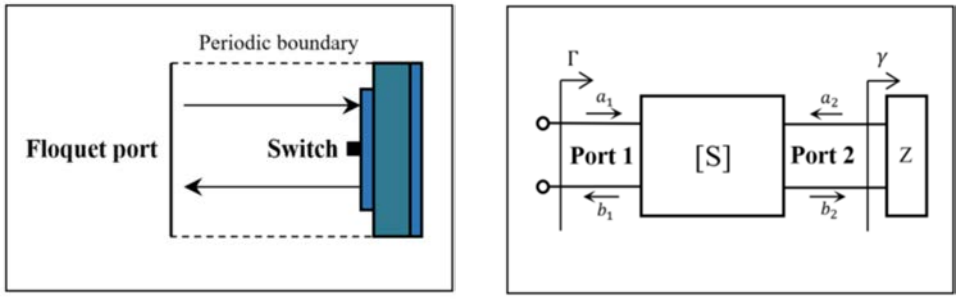

(a) Schematic of an RIS element **(b) Equivalent two-port network model of the RIS element**

Figure 6.2.1-1: Model of an RIS element with a single switch

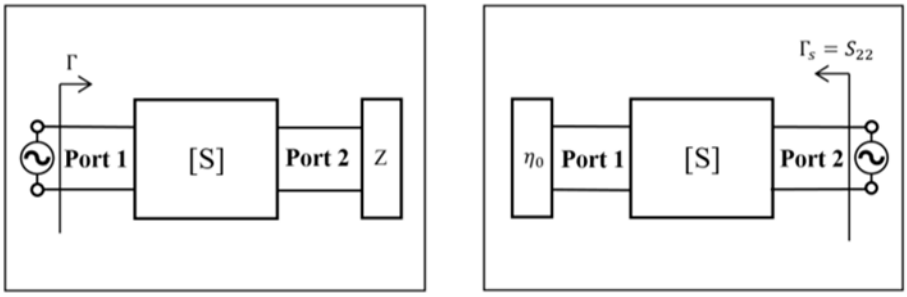

(a) Scattering viewpoint **(b) Radiation viewpoint**

Figure 6.2.1-2: Two understandings of an RIS element under network equivalence

Based on the observations above, two ways are compared to understand an RIS element, as shown in Figure 6.2.1-2. The traditional and straightforward approach views the antenna structure with the multistate switch as a scattering structure. The passive structure and active switch are treated as a single entity that scatters the incident wave, as shown in Figure 6.2.1-2(a).

The key insight is that Figure 6.2.1-2(b) also represents the equivalent model of a classical single-port radiation antenna. Under a radiation viewpoint, the scattering RIS structure is converted to a classical radiation antenna structure through network equivalence. This allows the systematic and advanced impedance matching techniques used in radiation antenna design to be applied to RIS element design now. It is noted that this model is based on the assumption of a lossless passive antenna structure. Using this viewpoint, the design goal is to match the element impedance to a characteristic impedance pre-calculated by switch parameters, allowing various impedance matching techniques developed in classical antennas to be applied in RIS element design. Furthermore, the theoretical performance limit can be predetermined at given switch parameters before designing specific structures. Accurate modelling can accurately estimate the reflective performance of RIS elements, which plays an important supporting role in near-field channel estimation.

The scattering viewpoint applies to both far field and near field, while in near field, the radiation viewpoint can better match the reflective element and its spatial impedance, thus, better characterizes the near field propagation for RIS.

6.3 Channel model of RIS-aided near-field system

6.3.1 Near-field path loss model

The near-field effect is widely present in wireless communications on high frequencies, such as sub-THz and THz. The pathloss model for the near-field needs to be studied clearly for the purpose of establishing a channel model for RIS-assisted communications at high frequencies such as sub-THz and THz.

Due to the high frequency and short wavelength, the high transmission loss of high-frequency communication results in a short coverage distance, while the limited diffraction capability causes the transmission to rely on the LoS path. However, a LoS link can easily be blocked (such as at THz bands), leading to high-speed communication interruption. As such, RIS has become an innovative and cost-effective choice to provide a virtual LoS link.

Assuming free-space propagation and applying the image theory [i.16], it can be shown that the signal power received at the receiver via the reflection of an infinitely large Perfect Electric Conductor (PEC) (or metallic plate), denoted by $P_{r,PEC}$, is inversely proportional to the square of the sum distance of the two-hop links, i.e.:

$$P_{r,PEC} \propto \frac{1}{(d_1+d_2)^2}.$$

This model is usually referred to as the sum-distance path loss model. In existing literatures, it is discussed that when the transmitter is in the near field of the RIS, it means that the transmitter is relatively near to the RIS, thus the electromagnetic wave transmitted to the RIS can be regarded as a spherical wave. Specifically, when the maximum phase difference of the received signal on the antenna array exceeds $\frac{\pi}{8}$, the transmitter is in the near-field of the antenna array. Based on this assumption, the boundary of the far field and the near field of the antenna array is defined as:

$$L = \frac{2D^2}{\lambda},$$

where L, D, and λ denote the distance between the transmitter and the center of the antenna array, the largest dimension of the antenna array and the wavelength of the signal.

If the RIS is electrically large (i.e. both of its length Mdx and width Ndy are at least 10 - 100 times larger than the wavelength λ depending on the setup):

$$\min(Mdx, Ndy) > 100\ \lambda,$$

then the incident spherical wave forms a circular and divergent phase gradient on the RIS surface, which is due to the different transmission distances from the transmitter to each unit cell of the RIS. Then, the received signal power, denoted by P_r, through the reflection of an RIS of large electrical size in the near-field case can be also considered inversely proportional to the square of the sum distance of the two-hop links, i.e.:

$$P_r \propto \frac{1}{(d_1+d_2)^2},$$

instead of ${d_1}^2{d_2}^2$ in the far-field case.

It is worth noting that, in THz band, the near-field region expands as the wavelength of the signal dramatically decreases. For example, for a 5×5 cm^2 RIS, if the operating frequency is 3 GHz, the near-field region is 0,1 m, whereas if the operating frequency is 300 GHz in THz band, the near-field region is 10 m. This means that when the receiver is within 10 m but larger than a threshold, the RIS cannot be considered electrically large in the same way it is within 0,1 m at lower frequencies (at lower frequencies, sum-distance path-loss model holds within the whole near field region). As a result, the free-space path loss of RIS-assisted THz channel is not proportional to $(d_1 + d_2)^2$ in the whole near-field region. In fact, in RIS-assisted THz systems, different pathloss models should be considered for different regions of near-field. As seen in Figure 6.3.1-1, denote *S* as the distance of the RIS-user link such that the RIS is electrically large as seen from the user, and *L* as the Rayleigh distance of the RIS. For distance less than *S*, the power scaling laws follows the sum-distance path-loss model. For distance greater than S and less than L, the power scaling laws follows the product-distance path-loss model. For distance greater than S, i.e. far-field of the RIS, the power scaling laws also follows the product-distance path-loss model.

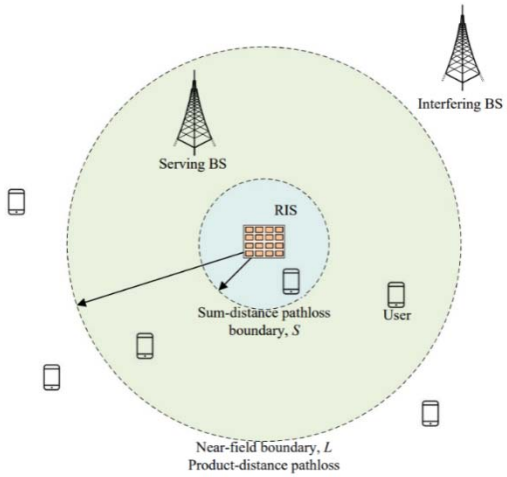

Figure 6.3.1-1: Near-field effect of the RIS

In addition, the molecular absorption starts to significantly impact the propagation loss in high-frequency communication, especially at a frequency around 60 GHz (oxygen) and above 300 GHz (water vapor). Specifically, the THz propagation spectral lines are separated by the molecular absorption peaks into multiple transmission windows, which is a notable distinction compared to the millimeter-wave (mmWave) counterpart. Such molecular absorption relates to the pressure, temperature, temperature of the transmission environment. Also, the total number of molecules per unit volume and the absorption cross section for the isotopologue of different gas at different frequency take effect. Thus, the RIS reflection propagation model should be separately established according to unique molecular absorption at different THz sub-bands.

From the perspective of signal characterization and EM response, the following points need to be considered for RIS-assisted high-frequency communication systems. First, the impact of the ultra-massive MIMO antenna on the near-field range cannot be ignored. Second, non-ideal RIS hardware response (e.g. the effect of temperature on reflection characteristics and phase response with errors) should be considered at the theoretical level. Third, the RIS reflection propagation model should account for unique diffraction/scattering ability and molecular absorption.

6.3.2 Near-field channel model

As introduced in ETSI GR RIS 003 [i.3], there are different types of RIS models, e.g. modeled as the mutually-coupled antenna model, modeled as a continuous surface sheet through surface functions, are introduced. Considering these different RIS models, the channel model of RIS-aided near-field system can be introduced, respectively. And in the existing study of 3GPP Release 19 for FR3 channel model [i.9], [i.8], the methodology of near-field channel model is discussed.

- Array-based RISs

For the array-based RIS, RISs are composed of numerous low-cost elements that are independently configurable (by an external controller) through tuneable impedances [i.8]. The RIS-aided near-field MIMO channel can be accurately modeled using a channel matrix having dimension equal to the number of transmit and receive antennas. With each entry (i, j) of near-field channel is given by [i.13]:

$$\left[G^{LOS}\right]_{i,j} = \sum_{m=1}^{M} \beta_{i,j,m} e^{-j2\pi\left(\left\|\mathrm{r}_i - \mathrm{s}_m\right\| + \left\|\mathrm{s}_m - \mathrm{t}_j\right\|\right)} = \sum_{m=1}^{M} \beta_{i,j,m} e^{-j2\pi\left\|\mathrm{r}_i - \mathrm{s}_m\right\|} e^{-j2\pi\left\|\mathrm{s}_m - \mathrm{t}_j\right\|}$$

where $\beta_{i,j,m}$ denotes the distance-dependent path loss of a cascaded link, which can be the cascaded path loss that is related to the distance between the antenna element of BS and RIS elements, and the RIS elements and antenna elements of UE; s_m denotes the Cartesian coordinate of the *m*-th RIS elements, $\mathrm{r}_i, \mathrm{t}_j$ denotes the Cartesian coordinates of the i-th receive antenna and j-th transmit antenna respectively, and for convenience of description, the distance and coordinates are normalized by the carrier wavelength λ. In this channel model, the RIS is in a shape of rectangular, and it can also be extended to other shapes.

The coordinates of the m-th RIS elements can be represented by $\left(x_{n_1}, 0, z_{n2}\right)$, where:

$$x_{n_1} = \left(n_1 - \frac{N_1 + 1}{2}\right)d, z_{n_2} = \left(n_2 - \frac{N_2 + 1}{2}\right)d$$

where the vertical or horizontal distance between two adjacent RIS elements is set to d and:

$$n_1 = 1, \cdots, N_1, n_2 = 1, \cdots, N_2.$$

Considering the large RIS aperture, the channel between the RIS and users are the near-field channel, which should be derived based on the spherical wave assumption, and can be represented by:

$$\left\|r_i - s_m\right\| = \sqrt{\left(x_r - x_{n_1}\right)^2 + y_r^2 + \left(z_r - z_{n_2}\right)^2}$$

which represents the distance from *m*-th RIS elements to the *i*-th receive antenna with coordinates $\left(x_r, y_r, z_r\right)$.

Similarly, the array steering vector at the RIS of the channel from the BS to the RIS can also be near-field, i.e. the distance between the *j*-th transmit antenna with coordinates $\left(x_{G_t}, y_{G_t}, z_{G_t}\right)$ to the *m*-th RIS element can be represented as following:

$$\left\|s_m - t_j\right\| = \sqrt{\left(x_{G_t} - x_{n_1}\right)^2 + y_{G_t}^2 + \left(z_{G_t} - z_{n_2}\right)^2}$$

According to the above equation, it can be observed that the near-field channel model has non-uniform channel gains and nonlinear phases.

6.3.3 Piecewise far-field channel model

The non-linear phase of the near-field channel model makes it intractable to devise near-field wideband beamforming techniques. It is observed that the Rayleigh distance $L = \frac{2D^2}{\lambda} = 2N^2\lambda$ scales proportionally with the square of the number of elements, given that the RIS elements are spaced $\lambda/2$. Inspired by such observation, a piecewise far-field channel model is proposed to approximate the intricate near-field channel. In this model, the entire RIS is partitioned into multiple sub-surfaces, each equipped with fewer reflection elements. Consequently, even if the transceiver is inside the near-field region of the entire RIS, it can be reasonably assumed that the transceiver is situated in the far-field region of each sub-surface.

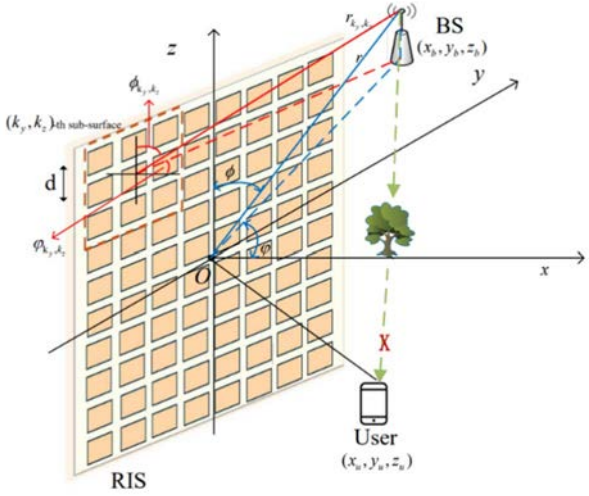

Figure 6.3.3-1: Piecewise far-field channel model illustration

Taking the BS-RIS channel as example, as shown in Figure 6.3.3-1, it divides the RIS into K sub-surfaces, with K_y sub-surfaces along the y-axis and K_z sub-surfaces along the z-axis, i.e. $K = K_y \times K_z$. It is assumed that each sub-surface contains the adjacent $S \times S$ elements that share a common delay, satisfying $S = N_y/K_y = N_z/K_z$. Assume that the RIS is centered at the origin, the coordinate of the center of $\left(k_y, k_z\right)$-th sub-surface is then expressed as $\left(0, \left(k_y - \frac{K_y-1}{2}\right)Sd, \left(k_z - \frac{K_z-1}{2}\right)Sd\right)$. Let r be the distance between the center of RIS and the BS, which can be written as $r = \sqrt{x_b^2 + y_b^2 + z_b^2}$. Then, the distance between the BS and the center of $\left(k_y, k_z\right)$-th sub-surface can be written as:

$$r_{k_y,k_z} = \sqrt{x_b^2 + \left(y_b - \left(k_y - \frac{K_y-1}{2}\right)Sd\right)^2 + \left(z_b - \left(k_z - \frac{K_z-1}{2}\right)Sd\right)^2}$$

$$= \left(r^2 + \left(\left(k_y - \frac{K_y-1}{2}\right)Sd\right)^2 - 2\left(k_y - \frac{K_y-1}{2}\right)Sdr\sin(\varphi)\sin(\phi) + \left(\left(k_z - \frac{K_z-1}{2}\right)Sd\right)^2 - 2\left(k_y - \frac{K_y-1}{2}\right)Sdr\cos(\varphi)\right)^{\frac{1}{2}}$$

where ϕ and $\varphi$are the azimuth and elevation angles of the BS with respect to (w.r.t.) the center of the RIS, respectively.

To this end, the distance $r_{s_y,s_z}^{k_y,k_z}$ between the BS and the $\left(s_y, s_z\right)$-th element, with $s_y, s_z \in S \triangleq \{1, \ldots, S\}$, of the $\left(k_y, k_z\right)$-th sub-surface can be expressed as:

$$\mathrm{r}_{s_y,s_z}^{k_y,k_z} = \left(\mathrm{r}_{k_y,k_z}^2 + \left(\left(s_y - \frac{S-1}{2}\right)d\right)^2 - 2\left(s_y - \frac{S-1}{2}\right)d r_{k_y,k_z}\sin\left(\varphi_{k_y,k_z}\right)\sin\left(\phi_{k_y,k_z}\right) + \left(\left(s_z - \frac{S-1}{2}\right)d\right)^2 - 2\left(s_z - \frac{S-1}{2}\right)d\, r_{k_y,k_z}\cos\left(\varphi_{k_y,k_z}\right)\right)^{\frac{1}{2}}$$

$$\approx r_{k_y,k_z} - \left(s_y - \frac{S-1}{2}\right)d\sin\left(\varphi_{k_y,k_z}\right)\sin\left(\phi_{k_y,k_z}\right) - \left(s_y - \frac{S-1}{2}\right)d\cos\left(\varphi_{k_y,k_z}\right),$$

where ϕ_{k_y,k_z} and φ_{k_y,k_z} are the azimuth and elevation angles of the BS w.r.t. the center of (k_y, k_z)-th RIS sub-surface, respectively, satisfying:

$$\sin\left(\phi_{k_y,k_z}\right) = \frac{y_b - \left(k_y - \frac{K_y-1}{2}\right)Sd}{\left(x_b^2 + \left(y_b - \left(k_y - \frac{K_y-1}{2}\right)Sd\right)^2\right)^{\frac{1}{2}}}$$

$$\sin\left(\varphi_{k_y,k_z}\right) = \frac{\left(x_b^2 + \left(y_b - \left(k_y - \frac{K_y-1}{2}\right)Sd\right)^2\right)^{\frac{1}{2}}}{r_{k_y,k_z}}$$

$$\cos\left(\varphi_{k_y,k_z}\right) = \frac{z_b - \left(k_z - \frac{K_z-1}{2}\right)Sd}{r_{k_y,k_z}}.$$

The approximation holds due to the first-order Taylor expansion $(1+x)^{\frac{1}{2}} \approx 1 + \frac{1}{2}x$ and the ignorance of:

$$\left(\left(s_y - \frac{S-1}{2}\right)d\right)^2 \text{ and } \left(\left(s_z - \frac{S-1}{2}\right)d\right)^2.$$

Accordingly, the normalized near-field channel model between the BS and the (s_y, s_z)-th RIS element in the (k_y, k_z)-th sub-surface is approximated as $\tilde{g}_m$, whose entries are given by:

$$[\tilde{g}_m]_{s_y,s_z}^{k_y,k_z} = e^{-j2\pi\frac{fm}{c}r_{k_y,k_z}} e^{j2\pi\frac{fm}{c}\left(\left(s_y - \frac{S-1}{2}\right)d\sin\left(\varphi_{k_y,k_z}\right)\sin\left(\phi_{k_y,k_z}\right) - \left(s_y - \frac{S-1}{2}\right)d\cos\left(\varphi_{k_y,k_z}\right)\right)}.$$

It is notable that the phase of the approximated model is a linear function of RIS element index. This linear phase property suggests that such model can be regarded as a far-field channel. Furthermore, considering the different distances and angles in each sub-surface, the planar waves impinging on different sub-subsurface come from different directions. This is why it is called piecewise-far-field channel. It provides a simplification of the non-linear phase in the near-field channel while maintaining accuracy, allowing further beamforming design strategy.

7 Technical challenges and solutions of RIS-aided near-field system

7.1 General introduction

The development of near-field communication technology has opened up new opportunities and challenges for RIS-aided communication. RIS have the characteristics of large array size and distributed deployment, which makes near-field communication gradually become one of the mainstream scenarios for RIS-aided communication in the future. Effective use of near-field channels can not only improve spatial resolution, but also improve multi-user multiplexing efficiency, providing strong support for emerging applications. However, this also brings many challenges, such as increased complexity of signal processing, increased overhead of pilot signals and beam training, increased complexity of codebook design, and increased complexity of deployment and networking design.

In this clause, the technical challenges and solutions on channel estimation, beamforming and beamfocusing, codebook design and other mechanisms are elaborated and studied. The potential specification impact can also be provided and analysed.

7.2 Channel estimation mechanism

7.2.1 Coupling phenomenon of near-field channel parameters

Near-field effects often emerge in RIS-assisted communication scenarios, primarily for two reasons. First, the RIS can provide virtual line-of-sight links for communication, effectively overcoming high-frequency signals' poor diffraction capability. Meanwhile, since RIS contains no RF chains and has lower manufacturing costs, RIS arrays are generally ultra-large-scale. As the near-field range is inversely proportional to wavelength and proportional to array size, RIS exhibits larger near-field regions where near-field phenomena occur more readily. Second, system performance improves when RIS is deployed closer to either the base station or user terminal, further increasing the likelihood of near-field effects in RIS-assisted systems.

In high-frequency scenarios where channels exhibit sparse characteristics with limited scattering paths, the received signal power becomes predominantly governed by the Line-Of-Sight (LoS) component. By treating scattering paths as part of the noise term, the received signal of a MISO system can be formulated as:

$$y = \rho e^{-jk(p_1 n^2 d^2 + p_2 nd)} + n_\sigma ,$$

where ρ is the amplitude of received signal. p_1 and p_2 are two parameters of the LoS channel which can be written as:

$$p_1 = \frac{\cos^2 \theta}{2r}, \quad p_2 = -\sin\theta ,$$

where θ and r are the elevation and distance from the user to the array reference antenna, respectively.

As shown above, whether utilizing parameter pairs p_1 and p_2 or θ and r to characterize near-field channels, inherent variable coupling phenomena persist. Current methodologies struggle to design convolutional kernels with separability or orthogonal decomposition mechanisms capable of decoupling parameters p_1 and p_2 into independent variable components. This intrinsic coupling characteristic in near-field parameters poses substantial challenges for channel parameter estimation, terminal positioning, and codebook design. Consequently, there is an urgent need to explore novel data processing methodologies that enable explicit decoupling of multidimensional parameters in near-field scenarios.

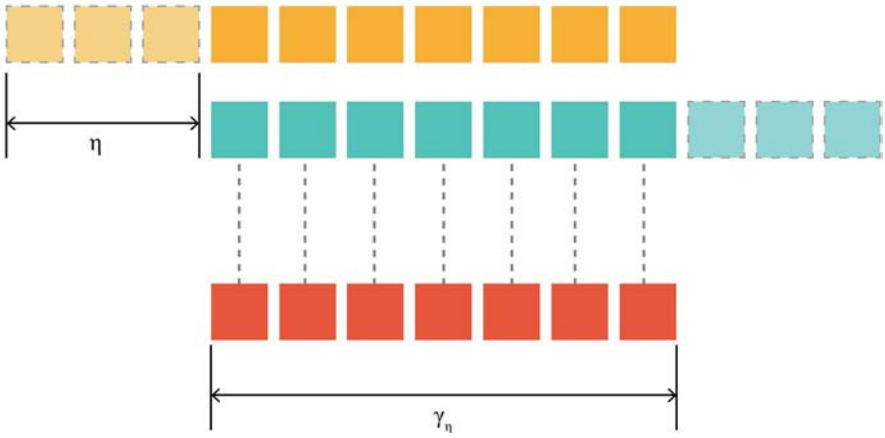

Figure 7.2.1-1: Construction of Equivalent Far-Field Signal

To address such parameter coupling issues, the two-dimensional estimation problem involving parameters p_1 and p_2 can be transformed into a two-step estimation process. When estimating parameter p_1 , an equivalent signal γ_η can be constructed through spatial autocorrelation operations. As shown in Figure 7.2.1-1, the orange blocks represent the received signals on the original antenna array. By applying a shift of length η to these signals, the shifted signals (blue blocks) are generated. Conjugate multiplication of the original signals (orange) and the shifted signals (blue) yields a new signal γ_η, which can be expressed as:

$$\gamma_\eta = 2\rho e^{-jk2p_1\eta nd} + n_{\sigma'}$$

where $n_{\sigma'}$ is the equivalent noise. It can be seen that the signal γ_η is now determined only by the parameters η and p_1. Among these, η is a manually controlled parameter and is known information, so the only unknown parameter in γ_η is p_1. Therefore, by constructing the signal γ_η, decoupling between p_1 and p_2 is achieved.

Additionally, it can be observed that γ_η, from a mathematical perspective, represents a far-field signal. Therefore, the process of estimating parameter p_1 is equivalent to far-field AoA estimation. Traditional far-field estimation algorithms can be directly applied to the estimation model for parameter p_1. After completing the estimation of p_1, one can substitute p_1 into the original received signal y, leaving p_2 as the only unknown parameter. The mathematical form of p_2 also corresponds to a far-field signal, allowing the system to again utilize far-field AoA estimation algorithms to estimate p_2. Ultimately, the coupled parameter estimation problem in the near field is transformed into two sequential far-field AoA estimation tasks. Although RIS itself lacks signal processing capabilities, parameter decoupling in near-field scenarios provides algorithmic-level insights for addressing RIS-related near-field challenges. Moreover, the essence of near-field parameter decoupling lies in transforming near-field signals into far-field forms, which also inspires future hardware design for RIS.

7.3 Beamforming and beamfocusing mechanism

7.3.1 Beam squint effect in RIS-aided near-field systems

RIS operating in the high frequency bands (such as sub-THz and THz bands) has recently gained considerable interest due to its high spectrum bandwidth. Due to the exploitation of the large scale of the RIS, there is a high probability that the transceivers will be situated within the near-field region of the RIS. Thus, the near-field beam squint effect poses a major challenge for the design of wideband RIS beamforming, which causes the radiation beam to deviate from its intended location, leading to significant gain losses and limiting the efficient use of available bandwidths. Besides, for a RIS-aided high-frequency communication with massive antennas at the Base Station (BS), the beam misalignment leads to the double beam squint effect. Specifically, the generated beams of the BS with massive antennas at different subcarriers point to different physical directions, which cannot be aligned with the RIS. Besides, the impinging beams and the reflected beams of the RIS cannot be aligned with the BS and the user in the whole bandwidth, respectively, which also squint into separated physical directions. In the following, several solutions to alleviate the beam squint effect in RIS-aided near-field systems are introduced, as illustrated in Figure 7.3.1-1.

Due to the beam squint effect, the frequency-independent beamformer generated by the frequency-independent Phase Shifters (PSs) in the conventional hybrid precoding architecture, will result in severe array gain loss. A new precoding architecture called Delay-Phase Precoding (DPP) can solve this problem. As shown in Figure 7.3.1-1(a), compared with the conventional hybrid precoding architecture, a Time Delay (TD) network is introduced as a new precoding layer between the RF chains and the frequency-independent PS network in the proposed DPP. Specifically, each RF chain is connected to K TD elements, and then each TD element is connected to $P = \frac{N_t}{K}$ PSs in a sub-connected manner. Therefore, each RF chain still connects to every antenna element through the PSs. The TD network can realize frequency-dependent phase shifts through time delays, e.g. the phase shift $-2\pi f_m t$ can be achieved by the time delay t at the subcarrier frequency f_m. Thus, by utilizing the TD network, the proposed DPP converts the traditional phase-controlled beamformer into delay phase jointly controlled beamformer, which can realize the frequency-dependent beamforming.

Inspired by the above DPP solution in wideband high-frequency communications, a sub-connected architecture for RIS is preferred. Nevertheless, the sub-connected architecture cannot be directly utilized for RIS. Specifically, the sub-connected BS is separated into several sub-arrays and each sub-array is connected to a TD module. Thus, the elements in a sub-array can provide the desired time delay. However, if the sub-connected delay-phase architecture is directly applied to RIS, the received signals at sub-arrays will first pass through the common TD module and will be mixed together incoherently. The possible resultant destructive interference would lead to severe signal attenuation. Thus, the sub-connected delay-phase architecture with an additional TD module for each sub-array of RIS is infeasible in practice. To tackle this problem, additional phase shifters to the sub-connected Phase-Delay-Phase (SPDP)-based RIS can be beneficial, as shown in Figure 7.3.1-1(b). Specifically, each element of the sub-array is equipped with two-layer phase shifters and is connected to a common TD module based on a circulator. The received signal at each element first passes through the first-layer phase shifter, which aims at creating constructive received signal superposition at the subarray. Then, the signal is adjusted by the common TD module. Finally, the signal passes through the second-layer phase shifter to accomplish the beamforming of the RIS. In practice, the proposed SPDP-based RIS can also be implemented by exploiting two smaller patches instead of one patch in each antenna based on the planar inverted-F antenna. Besides, the SPDP-based RIS can be implemented as a transmission array, where two-layer phase shifters can be deployed at two sides of the array, respectively.

With a large number of antennas at the transmitter or receiver, not all antennas of the receiver simultaneously receive the signals, because there are signal delays among different antennas. In addition, for the low-frequency multiple carriers, the ratio f_m/f_c can be approximated as 1, where f_m and f_c stand for the m-th and central subcarrier frequency, respectively. However, for THz, the above approximation will not hold. Meanwhile, the selection of the space among adjacent antennas usually depends on the wavelength of the central subcarrier frequency. Based on the above, the beamforming of the different subcarrier signals will generate different directions referred to as beam squint. Furthermore, more antennas (elements) at the BS (RIS) lead to longer signal delay among different antennas (elements) at the BS (RIS), which further amplifies the beam squint's effects. Generally, the RIS is a planar structure, and the horizon and elevation directions can both form the beam squint, aggravating the effects. Thus, the RIS deployments (sizes) also contribute to the beam squint effects. As shown in Figure 7.3.1-1(c), the large central RIS deployment (i.e. Scheme 1), distributed multiple rectangular RIS deployment (i.e. Scheme 2), distributed multiple square RISs (i.e. Scheme 3), and distributed large-scale square RIS deployment (i.e. Scheme 4) lead to different beam squint effects. It has been verified that Scheme 4 owns the smallest beam squint effects, but the deployment cost will be high. The frequency-dependent shifts realized by the TD module can help mitigate beam squint. However, when larger RIS structures are used, the maximum resulting propagation delay between the RIS elements may be comparable with the channel's delay spread. This spatial-wideband effect may need to be taken into account when, e.g. the total delay spread from the combined channel and TD module exceeds the limit posed by the numerology, thus reducing the effectiveness of beamforming and beamfocusing.

Since the antennas are deployed at fixed positions, conventional MIMO and massive MIMO cannot fully explore the spatial variation of wireless channels in a given receive area or receive field. To overcome this limitation, a new antenna architecture, namely Movable Antenna (MA), is proposed, for exploiting the DoFs in the continuous spatial domain more efficiently, as shown in Figure 7.3.1-1(d). Different from conventional Fixed-Position Antennas (FPAs), the positions of MAs can be flexibly adjusted in a spatial region for improving the channel condition and enhancing the communication performance. Note that the squinted beam pattern is related to the path delay between each antenna and user, which can be affected by the positions of antennas. Hence, the beam squint effect could be alleviated via delicately configuring MAs' positions, in other words, the analog beamforming among different frequencies can be improved. It has been verified that deploying MA array in wideband systems can significantly suppress the severe beam squint effect via appropriately configuring the position of each MA. Hence, the BS and/or the RIS equipped with movable antennas or sub-surfaces for beam squint effect mitigation may be a feasible solution.

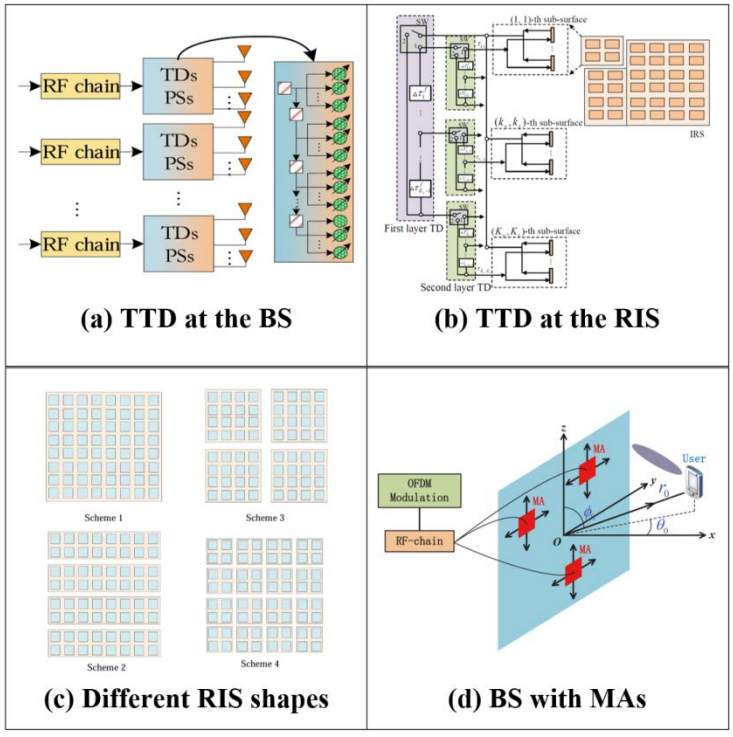

Figure 7.3.1-1: Beamforming strategies for RIS-aided near-field systems

7.3.2 Beamforming in dual near-field scenarios

"Dual near-field" refers to a scenario where both the base station and the Intelligent Reflecting Surface (IRS) are within each other's near-field regions. In contrast, "single near-field" describes a configuration where one device is in the near-field of the second device, while the second device resides in the far-field of the first. Since both the IRS and Base Station (BS) typically employ large-scale arrays, IRS-assisted communication scenarios are more prone to dual near-field issues compared to direct BS-user service scenarios. This challenge becomes particularly non-negligible in centralized deployments where the IRS is positioned in close proximity to the BS.

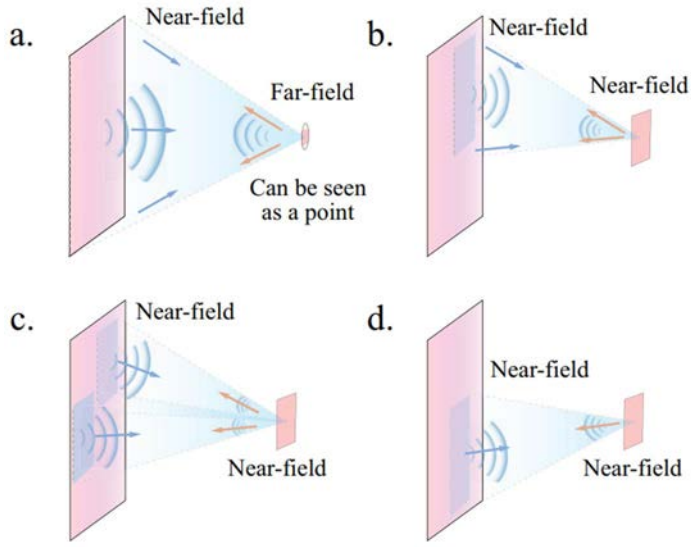

Figure 7.3.2-1: The visible region selection problem in dual near-field scenarios

For dual near-field beamforming problems, a virtual focal point can be introduced to optimize the beamforming design. Both the BS and IRS beams are focused on a specific spatial point. By optimizing the position of this virtual point, the mutual Visibility Regions (VR) between the two arrays can be maximized. This approach unifies the beamforming designs of the BS and IRS through the virtual point's coordinates. During the optimization of the virtual point's location, the beamforming patterns of both arrays evolve synchronously, effectively resolving the non-convergence issue in iterative algorithms for dual near-field scenarios.

In dual near-field beamforming systems, the inherent coupling between phase compensation of incoming waves and VR region selection creates optimization convergence challenges. To address this interdependency, the introduction of virtual point sources fundamentally transforms the problem structure. Specifically, the beamforming design objective shifts to compensating for phase differences between the array and these constructed virtual sources, while VR region selection translates into determining optimal virtual source positioning. This decoupling establishes distinct optimization targets: virtual source locations are optimized to maximize received power at the terminal array, and beamforming calculations focus solely on phase cancellation relative to the virtual references, thereby eliminating the need for precise knowledge of actual incoming wave characteristics. The unified framework enables separate yet coordinated optimization of these originally intertwined subproblems:

- Limitations: When the BS and IRS have small-scale apertures, their transmitted and received beams exhibit significant diffraction effects. Diffraction prevents precise electromagnetic energy focusing on a single point, introducing suboptimal performance.
- Practical Viability: In real-world engineering applications, dual near-field scenarios typically involve Extremely Large-Scale Arrays (ELAA), where diffraction errors become negligible. Thus, this virtual-point-based scheme remains one feasible solution. Additionally, higher signal frequencies and larger array sizes further suppress diffraction, reducing its impact. Consequently, this optimization strategy is asymptotically optimal - approaching theoretical optimality as the frequency tends to infinity.

7.3.3 Wideband beam split effect

7.3.3.1 Beam split/squint and double beam split/squint effects

RIS operating in the high frequency bands (such as sub-THz and THz bands) has recently gained considerable interest due to its high spectrum bandwidth. Most existing RIS beamforming schemes do not perform well when the signal bandwidth is large, which is due to the fact that RIS is usually equipped with frequency-independent phase-shifting circuits, resulting in frequency-independent beamforming. This leads to the so-called beam split (also known as beam squint) issue in the RIS-aided wideband system. Due to the usage of a large aperture of the RIS (with respect to the wavelength used), there is a high probability that the transceivers will be situated within the near-field region of the RIS. This causes the near-field beam split effect, which is different from the far-field beam split effect. Specifically, the far-field beam split renders the beams reflected by RIS at different subcarriers pointing toward different directions, while the near-field beam split renders the beams reflected by RIS at different subcarriers pointing at different locations and most of the beams fail to focus on the user.

Consider an RIS-assisted wideband communication system, where the BS is located at $(x_{\mathrm{b}}, y_{\mathrm{b}}, z_{\mathrm{b}})$ and the user is located at $(x_{\mathrm{u}}, y_{\mathrm{u}}, z_{\mathrm{u}})$. The RIS is centered at the origin, with N_y elements along the y-axis and N_z elements along the z-axis, satisfying $N = N_y \times N_z$. Then, the coordinate of the (n_y, n_z)-th RIS element, with $n_y = \mathcal{N}_y \triangleq \{1, \dots, N_y\}$ and $n_z = \mathcal{N}_z \triangleq \{1 \dots, N_z\}$, is given by $\left(0, \Delta_{n_y}^{N_y} d, \Delta_{n_z}^{N_z} d\right)$, where $\Delta_a^b = a - 1 - \frac{b-1}{2}$. Both of the BS and the user are considered to be within the Fraunhofer distance of the RIS, i.e. $R = \frac{2D^2}{\lambda_c}$, where D is the maximum aperture of the RIS and λ_c denotes the corresponding signal wavelength. The center frequency is denoted by f_c and the bandwidth is denoted by B, which is equally divided into M subcarriers. Then, each subcarrier frequency can be denoted by $f_m = f_c + \frac{B}{M}\left(m - 1 - \frac{M-1}{2}\right)$, with $m = \mathcal{M} \triangleq \{1, \dots, M\}$. Then, the LoS near-field channel between the BS and the RIS at the m-th subcarrier is denoted as $h_m \in C^{N \times \mathbb{1}}$, whose entries are given by:

$$[g_m]_{n_y,n_z} = \frac{\alpha_m}{r_{n_y,n_z}} e^{-j2\pi \frac{f_m}{c} r_{n_y,n_z}},$$

where $\alpha_m \triangleq \frac{c}{4\pi f_m}$, $\frac{\alpha_m}{r_{n_y,n_z}^{n_t}}$ denotes the free-space path loss, and r_{n_y,n_z} denotes the distance between the n_t-th BS antenna and the (n_y, n_z)-th RIS element, which can be calculated as $r_{n_y,n_z}^{n_t} = \left(x_{\mathrm{b}}^2 + \left(y_{\mathrm{b}} - \Delta_{n_y}^{N_y} d\right)^2 + \left(z_{\mathrm{b}} - \Delta_{n_z}^{N_z} d\right)^2\right)^{\frac{1}{2}}$. Similarly, the LoS near-field channel between the RIS and the user at the m-th subcarrier is denoted as $h_m \in C^{N \times \mathbb{1}}$, whose entries are given by:

$$[h_m]_{n_y,n_z} = \frac{\alpha_m}{l_{n_y,n_z}} e^{-j2\pi \frac{f_m}{c} l_{n_y,n_z}},$$

where $l_{n_y,n_z} = \left(x_{\mathrm{u}}^2 + \left(y_{\mathrm{u}} - \Delta_{n_y}^{N_y} d\right)^2 + \left(z_{\mathrm{u}} - \Delta_{n_z}^{N_z} d\right)^2\right)^{\frac{1}{2}}$ represents the distance between the (n_y, n_z)-th RIS element and the user.

Define the array gain of the RIS at the m-th subcarrier as:

$$\eta(\mathrm{f_m}) = |\mathrm{h_m^T} \boldsymbol{\Theta} \mathbf{g_m}| = \left| \sum_{n_y=1}^{N_y} \sum_{n_z=1}^{N_z} e^{-j2\pi \frac{f_m}{c}\left(r_{n_y,n_z} + l_{n_y,n_z}\right)} e^{j\theta_{n_y,n_z}} \right|$$

The conventional narrowband RIS beamforming design aims at generating the reflected beams towards the target location. Such a RIS beamforming vector can be adopted based on f_c, expressed as:

$$\theta_{n_y,n_z} = \frac{2\pi}{\lambda_c}\left(r_{n_y,n_z} + l_{n_y,n_z}\right), n_y \in \mathcal{N}_y, n_z \in \mathcal{N}_z$$

Owing to the frequency-independent characteristic of RIS beamforming, the generated beams cannot perfectly point towards the target location in the whole bandwidth, which leads to severe gain loss. In Figure 7.3.3.1-1(a), it illustrates this by plotting the normalized array gain at f_c and two edge subcarriers, f_1 and f_M. It can be observed that the near8field beam split causes the beams at different subcarriers to split towards different locations. This restricts the user to receive signals that are only around the center frequency.

Further considering multi-antenna at the BS, then the array gain is defined as:

$$\eta(f_m) = |h_m^T \boldsymbol{\Theta} \boldsymbol{G_m} \boldsymbol{w}|$$

where $\boldsymbol{G_m} = \left[\text{vec}(\boldsymbol{g_m^1}), \cdots, \text{vec}(\boldsymbol{g_m^{N_t}})\right] \in C^{N \times N_t}$ and the entries of $\boldsymbol{g_m^{n_t}}$ are given by:

$$\left[g_m^{n_t}\right]_{n_y,n_z} = \frac{\alpha_m}{r_{n_y,n_z}^{n_t}} e^{-j2\pi \frac{f_m}{c} r_{n_y,n_z}^{n_t}}.$$

In this case, the beam misalignment leads to the double beam split effect. Specifically, the generated beams of the BS with massive antennas at different subcarriers point to different physical directions, which cannot be aligned with the RIS. Besides, the impinging beams and the reflected beams of the RIS cannot be aligned with the BS and the user in the whole bandwidth, respectively, which also split into separated physical directions. Thus, the RIS-aided wideband communication suffers from severe double array gain loss. In Figure 7.3.3.1-1(b), the double beam split effect in a RIS-aided near-field system has been plotted. Different from that in Figure 7.3.3.1-1(a), the array gain at edge subcarrier is degraded, which indicates the double array gain loss at the desired user position.

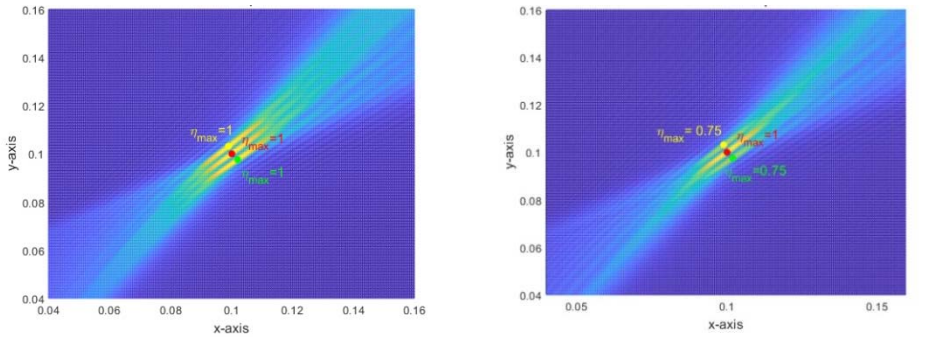

(a) the beam split effect **(b) the double beam split effect**

Figure 7.3.3.1-1

7.3.3.2 Potential solutions to double beam squint effect

As mentioned before, one prominent challenge of RIS-assisted wideband system is the double beam squint effect, which is derived from the multiplicative nature of analog beamforming gain at the BS and RIS. Specifically, when subcarrier frequency significantly deviates from the reference tone (e.g. central frequency), the analog beamforming gain at the BS and RIS severely degrades, which further impairs the array gain of BS-RIS-user link. As unveiled by the existing literature, beam squint effect can be remarkably alleviated by deploying a Movable Antenna (MA) array in wideband communication system. Inspired by the above observations, it can be motivated to investigate movable component implementation at both the BS and RIS to effectively combat double beam squint effect in a wideband system. To maintain low complexity and hardware cost at the RIS, the reflecting elements are grouped into multiple subarrays, each of which can flexibly move within the RIS surface. The movability can be achieved by both mechanical and electrical techniques. For the former, since the movability is achieved by moving the RIS elements through stepper motors or liquid metal techniques, the speed of movement is slow. Instead, via switching RIS elements on and off to yield movement virtually, the operation can be accomplished within few milliseconds or even microseconds by electrical techniques, which are suitable for practical communication systems.

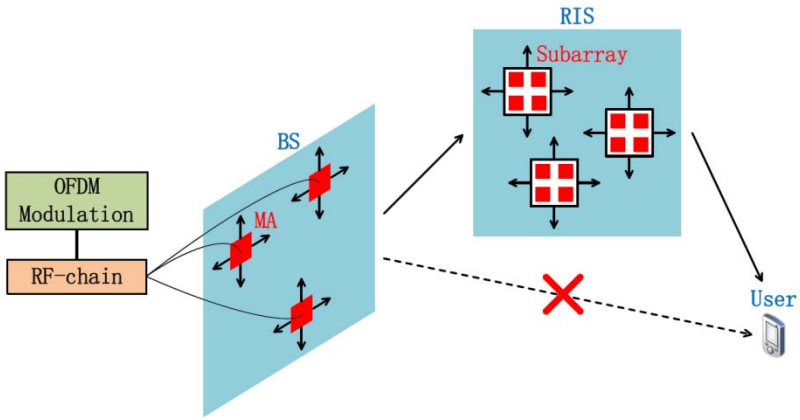

Figure 7.3.3.2-1: Wideband MISO MA-enabled communication system aided by an RIS with movable subarrays

As shown in Figure 7.3.3.2-1, since the double beam squint effect is caused by beam squint occurring at both the BS and RIS, it has been proposed to deploy the MA array at the BS and employ movable elements embedded in the RIS to suppress beam squint effect at the BS and RIS sides, respectively, and hence the double beam squint effect can be mitigated. Due to costly expenditure of element-wise movement at the RIS, it has been proposed to partition the RIS elements into subarrays with each moving freely.

To mitigate double beam squint effect, a max-min criterion has been proposed to jointly configure the MAs' and RIS subarrays' positions, which maximizes the minimal received power over a wide frequency band. Our formulated optimization problem is nonconvex due to the max-min form of the objective and the nonconvex constraints guaranteeing the avoidance of antenna coupling and subarray collision, which is difficult to solve.

To solve the above challenging optimization problem, an algorithm has been developed based on appropriate transformation and Majorization-Minimization (MM) framework. Specifically, the complicated objective can be equivalently transformed into some constraints by introducing a slack variable. Then, the Block Coordinate Descent (BCD) method has been utilized to obtain a more tractable solution, where all the nonconvex constraints will be tackled via MM methodology. Detailed derivations can be referred to [i.19]. Note that our proposed solution is suitable for fixed position users and mobile users. For the former, since the served device does not change its position (e.g. sensors and machines), the mechanical techniques for movability can be used and the positions of MAs need not to be reconfigured frequently (e.g. one day or even one week). For the latter, the electrical techniques need to be utilized to adapt to the fast movement of mobile users. In this case, the positions of MAs will change frequently (e.g. few seconds or even milliseconds).

Our proposed solution can completely eliminate the double beam squint effect by delicately adjusting all the movable components. Besides, appropriately enlarging the size of RIS subarray can lead to slight performance degradation compared to element-wise movement, but can achieve significant hardware cost and computational complexity reduction. In particular, Figure 7.3.3.2-2 plots the normalized array gain across different subcarriers operating in the considered frequency band, where the schemes considered in this figure are elaborated as follows:

i) Mov., BS+RIS: this is our proposed solution where the BS and RIS are equipped with MAs and movable subarrays, respectively.

ii) Mov., BS: the antennas at the BS can flexibly move while RIS elements cannot move.

iii) Mov., RIS: the BS employs traditional Fixed Position Antennas (FPAs) while the RIS consists of movable subarrays.

iv) Fixed, BS+RIS: both the BS and RIS are equipped with fixed position components.

As shown in Figure 7.3.3.2-2, due to RIS-aided wideband systems suffering from severe double beam squint effect, the normalized array gain of subcarriers at side frequencies significantly degrades if the BS antennas and RIS elements do not have any movability. This phenomenon emphasizes the necessity of applying movable components to the BS and RIS. Since the double beam squint effect results from the beam squint at both the BS and RIS, moving merely BS antennas or RIS subarrays cannot sufficiently suppress double beam squint effect. In contrast, it can be completely eliminated via appropriately configuring the positions of MAs and subarrays.

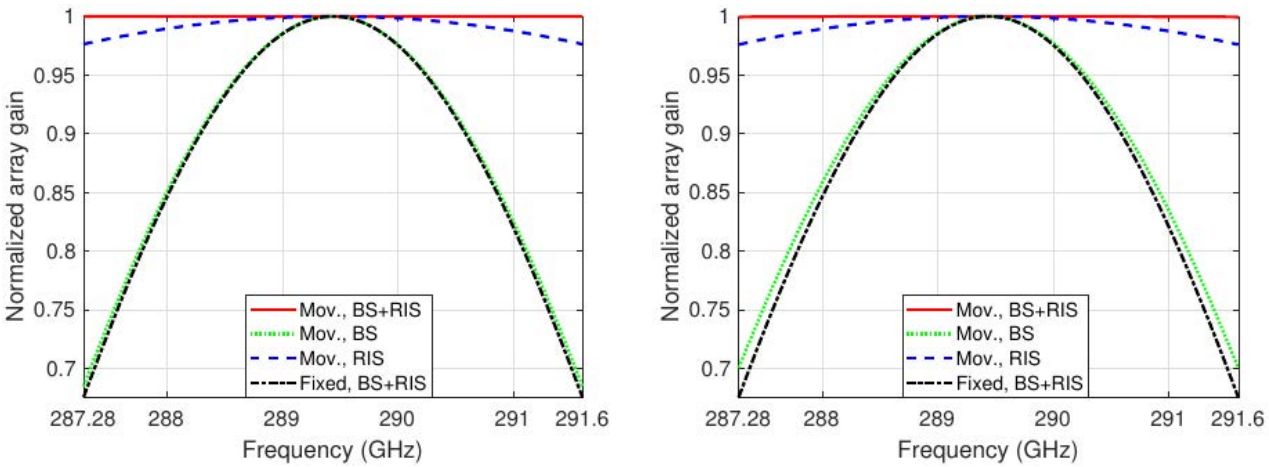

Figure 7.3.3.2-2: Normalized array gain across considered frequency band

7.3.4 Analytical Beam Shaping for Spatially Non-Stationary Near-Field Channels

Reconfigurable Intelligent Surfaces (RIS) are a foundational technology for future wireless networks, enabling software-defined control over the propagation environment. The relatively low cost of RIS makes the deployment of surfaces with a very large physical aperture practical. The vastness of such an aperture substantially increases the area where users are operating in the Near-Field (NF) regime, which introduces the critical challenge of spatial non-stationarity of the channel across the surface. This phenomenon arises because different physical segments of the surface may be illuminated by distinct propagation paths (e.g. line-of-sight or scattered paths), as scattering paths may only reach a fraction of the entire array. Consequently, the optimal wavefront required to maximize the received Signal-to-Noise Ratio (SNR) is not a simple, regular shape (like a plane or sphere), but rather a complex, piecewise function that conforms with the channel's spatial variations.

This poses a fundamental limitation to conventional beamforming techniques, which are implicitly designed for spatially stationary channels. The core research problem thus becomes as follows: Given a complex target wavefront dictated by the near-field channel's geometry, what is an efficient, non-iterative method to synthesize the corresponding phase configuration on the RIS? This proposal introduces a novel analytical framework to directly address this question.

The framework provides a direct synthesis engine that translates the physical geometry of a spatially non-stationary near-field channel into the required RIS phase configuration. The core idea is to first design a frequency-independent, continuous normalized phase function, and then sample it to obtain the final discrete physical phase shifts.

The synthesis process begins by modelling the channel's physical properties. The RIS surface is conceptually partitioned into segments, each being illuminated by a dominant propagation path with a distinct "visibility region". For each segment, its representative local geometry can be extracted: a direction θ_c and a distance r_c (to the user or a scatterer) at the segment's center, x_c.

This local geometry directly determines the required local behavior of the normalized phase function, $g(x)$. To achieve near-field focusing that matches the channel's wavefront, the second derivative (normalized curvature) and first derivative (normalized gradient) of the phase within that segment are given by [i.21]:

$$g''(x) = \frac{\cos^2 \theta_c}{r_c}$$

$$g'(x) = \sin \theta_c + \int_{x_c}^{x} g''(t)dt = \sin \theta_c + \frac{\cos^2 \theta_c}{r_c}(x - x_c)$$

By repeating this process for all segments, a complete, albeit piecewise can be constructed, function for the normalized phase gradient $g'(x)$ across the entire aperture. Crucially, this function $g'(x)$ is allowed to have discontinuities at the boundaries of the visibility regions, reflecting the abrupt changes in the channel's spatial characteristics.

The next step is to obtain the continuous normalized phase profile $g(x)$ by integrating the piecewise gradient function $g'(x)$. A critical constraint here is that the phase function $g(x)$ itself should be continuous across the entire aperture. A discontinuity in $g(x)$ would be physically interpreted as an infinite phase gradient, leading to undesired radiation. Therefore, starting from a reference phase $g(0)$ at the origin of the aperture, a continuous integration can be performed:

$$g(x) = g(0) + \int_0^x g'(t)dt$$

This integration ensures that even if the gradient $g'(t)$ is piecewise, the resulting phase profile $g(x)$ is connected and smooth, correctly representing the target wavefront.

The final step, termed "sampling," translates the continuous, normalized solution into a discrete, physical phase configuration for an RIS with N elements. This step involves two concurrent operations:

1) Discretization: The continuous position x is replaced by the discrete locations of the antenna elements, $x_n = (n-1)d$, where d is the inter-element spacing.

2) De-normalization: The normalized phase $g(x_n)$ is converted to the true physical phase ϕ_n by multiplying with the wavenumber $k = 2\pi/\lambda$.

The resulting physical phase shift for the n-th element, ϕ_n, is given by the analytical expression:

$$\phi_n = k \cdot g(x_n) = k\left(g(0) + \int_0^{(n-1)d} g'(t)dt\right)$$

The proposed analytical framework transforms the intractable problem of directly optimizing tens of thousands of phase shifts for a non-stationary channel into a direct and efficient calculation. By starting from the channel's physical geometry and systematically constructing the required phase profile through continuous modelling and integration, our method offers a flexible, scalable, and non-iterative solution for arbitrary wavefront synthesis in complex near-field environments. This provides a powerful tool for unlocking the full potential of RIS in future 6G networks.

7.3.5 Beam training design mechanism

For RIS-aided near-field communications, Channel State Information (CSI) estimation becomes quite challenging. This is because having a large number of RIS elements and transceiver antennas leads to high-dimensional channels. The corresponding complexity of estimating the complete CSI become excessive. Moreover, the passive nature of RISs makes the challenge even harder. As a remedy, beam training is proposed. Relying on a predefined codebook comprised of different RIS beamforming vectors representing specific angular beams, near-field beam training aims for determining the specific location of the target receiver both in terms of its angle and distance by selecting the optimal passive beamformer from the codebook that achieves the maximum received signal power. By doing so, a high-quality initial link can be established for CSI estimation of the cascaded BS-RIS-user channel with reduced dimension.

However, existing far-field beam training solutions are unsuitable for near-field beam training. This can be explained from the perspective of codebook design and training protocol. The codebook design is the core of beam training, which directly determines the ultimate accuracy. Upon recalling that the near-field channels require both angular and distance information (as illustrated in Figure 7.3.5-1), the angle-only codebooks developed for far-field beam training become inefficient due to the energy-spread effect. In particular, the energy of a far-field codebook designed for a specific angle will spread to a range of different angles in the near field. As a result, the accuracy of the far-field codebook becomes gravely degraded. Circumventing this requires a codebook tailored for near-field beam training, where the codebook has to cater for both the discrete angular domain and the discrete distance domain, i.e. in the polar domain. Hence, compared to the far-field codebook, the near-field codebook becomes much larger, which further increases the complexity of near-field beam training.

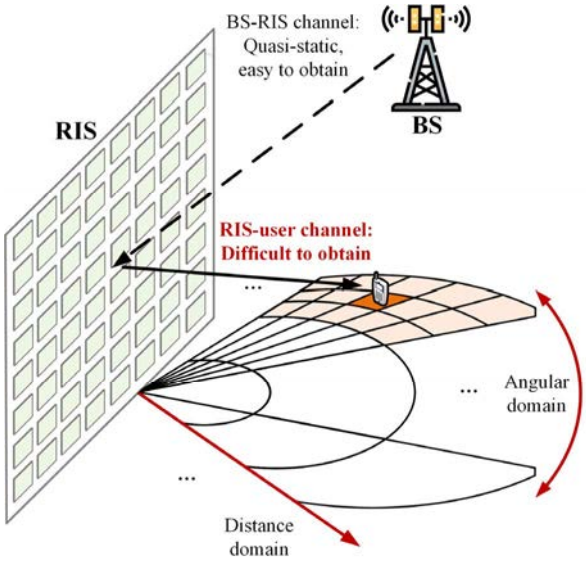

Figure 7.3.5-1: Beam training for RIS-aided near-field systems

To achieve efficient near-field beam training for RIS-aided near-field systems, as shown in Figure 7.3.5-1, the BS and RIS usually have fixed locations and thus have a (quasi) Line-Of-Sight (LoS) link between them. The corresponding BS-RIS channel is typically quasi-static in practice. The main challenge lies in the beam training of the RIS-user near-field channel. Exploiting the BS-RIS channel obtained, the BS's transmit beamforming can be directed towards the RIS. Then, the cascaded BS-RIS-user near-field beam training can be reduced to the RIS-user near-field beam training with the following two-stage hierarchical beam training approach.

This two-stage hierarchical beam training approach relies on initially activating a small central sub-array of the entire RIS during the beam training. Here, each RIS element consists of a specific circuit consisting of reconfigurable components, e.g. PIN diodes, which can be turned on or off for activation or deactivation. When the RIS elements are turned off, the incident signal will either pass through the surface [i.10] or be absorbed by the surface [i.11]. Therefore, only activated RIS elements will contribute to the reflection. The key idea is that upon activating a small sub-array, far-field propagation becomes dominant, and the near-field energy-spread effect is reduced [i.12]. As shown in [i.12] two stages are:

1) the coarse angular estimation stage of far-field communications; and

2) the joint angular and distance estimation stage.

The number of layers in stage 1 and stage 2 are denoted by L_1 and L_2, respectively. With the gradual increase of the number of layers, the number of activated RIS elements also increases exponentially until all elements become activated in the last layer. Through each layer, the activated RIS elements expand from the central region of the RIS to the entire surface. The total number of layers, $L = L_1 + L_2$, is determined by the total number of RIS elements denoted by N, i.e. $L = \log_2 N$. For each stage, the main procedure may be formulated as follows [i.13]:

1) **Stage-1 Coarse Angular Estimation:** As shown at the left of Figure 7.3.5-2, each layer only activates a relatively small number of RIS elements. In this case, the users can be regarded to be located in the far-field region of the RIS, where the near-field energy-spread effect is negligible. Therefore, the conventional hierarchical far-field codebook that only distinguishes the angular domain is employed for coarsely estimating the user's angular information. In stage 1, the reflection signal gain can be limited due to the relatively small number of activated RIS elements, e.g. only 2 activated RIS elements in the first layer. The corresponding reflection signal gain is sufficient since only two different angular beams need to be distinguished in each layer. Therefore, in each layer of stage 1, 2 possible angular codewords are used to divide by half the angular inaccuracy, as shown at the left of Figure 7.3.5-2.

2) **Stage-2 Joint Angular and Distance Estimation:** As shown at the right of Figure 7.3.5-2, given a reduced user angle candidate set estimated by stage 1, this stage further increases the number of activated RIS elements, hence near-field propagation becomes dominant. This stage then employs an appropriately designed hierarchical polar-domain codebook for jointly estimating the user's angular and distance information. In particular, each codeword within the hierarchical polar-domain codebook corresponds to a distinct combination of a sampled angular direction and a sampled distance. In each layer of stage 2, 4 possible polar-domain codewords are used to divide by half the angular and ranging inaccuracy, as shown at the right of Figure 7.3.5-2.

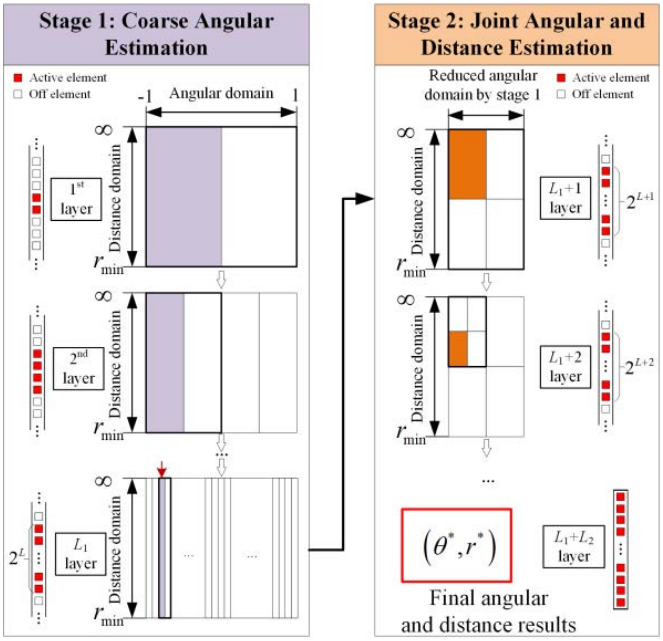

Figure 7.3.5-2: Two-stage hierarchical beam training for RIS-user near-field channels

7.3.6 Beamforming schemes with near-field and far-field users

To address the increasing demands for high data rates and extensive connectivity in beyond fifth-generation (5G) and sixth-generation (6G) networks, several innovative technologies have been developed. One of the most notable is extremely large-scale Multiple-Input Multiple-Output (XL-MIMO), which has gained significant interest. XL-MIMO takes a significant step forward from massive MIMO by increasing the number of antennas by at least ten times, ranging from several hundreds to thousands. This advancement enhances Spectral Efficiency (SE), Energy Efficiency (EE), and supports reliable massive connectivity. Additionally, the considerable increase in antennas improves spatial resolution, which leads to better spectrum usage and allows for higher peak data rates - key objectives for 6G.

The larger size of antenna arrays in XL-MIMO presents various challenges, as it significantly changes the Electromagnetic (EM) characteristics and requires careful design. In traditional massive MIMO, the received EM wave is usually treated as a plane wave, assuming users are located far from the array. However, in XL-MIMO, Near-Field (NF) propagation becomes more important since the Rayleigh distance, which serves as the boundary of NF region and Far-Field (FF) region, can be up to several hundreds of meters. For instance, if the array aperture is 0,4 m and the carrier is 100 GHz, then the Rayleigh distance is around 107 m, which covers a large part of a cell. Therefore, the EM field should be represented with spherical wavefronts. Moreover, there is spatial non-stationarity, meaning different sections of the array may exhibit different coverage of the environment. Consequently, a user may receive most of the power from a specific area of the array, referred to as the Visibility Region (VR).

On the other hand, in complex wireless environments, large objects can obstruct signal reception for some users. The RIS is a flat array containing many inexpensive passive elements, each of which can create a specific phase shift with the help of a smart controller connected to the RIS. By utilizing the ability of RISs to modify the wireless propagation environment, a promising strategy is to combine RISs with XL-MIMO systems, where the XL-MIMO system is at the Base Station (BS). RIS-assisted XL-MIMO systems are anticipated to leverage the advantages of both technologies, particularly when the direct links between the BS and users are blocked.

In the existing literature, a comprehensive analysis of RIS-assisted XL-MIMO, considering VR selection, phase shifts design, and power control, is still lacking, which motivates the study. Three linear precoding methods are examined - Maximum Ratio Transmission (MRT), Local Zero-Forcing (LZF), and Central Zero-Forcing (CZF) - in a RIS-assisted XL-MIMO downlink communication system with NF-Users (NFUEs) and FF-Users (FFUEs). It further assumes that FFUEs are blocked by some obstacles and are assisted by a RIS, as shown in Figure 7.3.6-1.

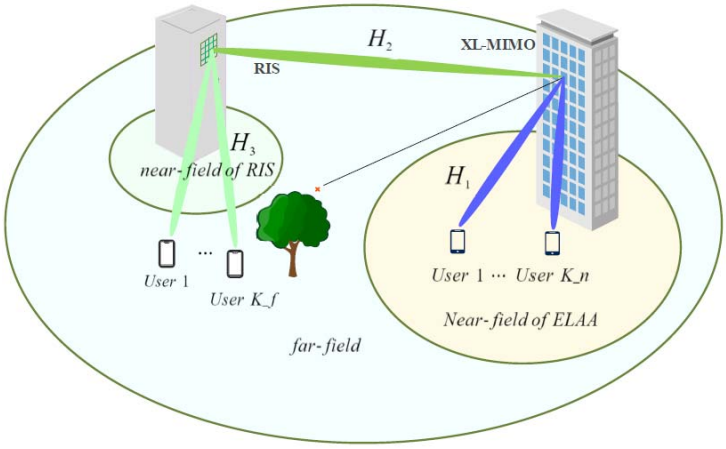

Figure 7.3.6-1: The considered XL-MIMO system assisted by a RIS

Based on these linear precoding schemes, a joint optimization problem has been considered that combines VR selection, phase shift design, and power control for MRT, LZF and CZF precoding schemes. The goal is to ensure consistently high service quality among groups of users. Our objective is to maximize the total weighted minimum SE for both NFUEs and FFUEs, while making sure that all users fulfil their Quality-of-Service (QoS) requirements. The advantage of our proposed optimization problem lies in that it not only considers the fairness between all users, but also enhances the stability of communication systems, especially in cases of network congestion or high load, a certain level of service received by all users can be ensured.

This complex non-convex optimization problem is reformulated into a simpler form with separated optimization variables. To accomplish this, a heuristic algorithm for selecting effective VRs for each user has been present. Next, a two-stage low-complexity algorithm has been developed by breaking down the non-convex problem into two subproblems. In the first stage, it introduces an algorithm for determining optimized phase shifts using the penalty method and Successive Convex Approximation (SCA). In the second stage, it proposes a power control algorithm based on SCA. Detailed discussions can be referred to [i.20].

Our study indicates that:

1) the optimized phase shifts and power allocation significantly enhance the overall weighted minimum SE for NFUEs and FFUEs;

2) CZF is generally the preferred method, while LZF performs comparably with lower complexity when both NFUEs and FFUEs are treated equally;

3) when priorities differ between NFUEs and FFUEs, LZF offers good performance for prioritized users, while CZF provides a more balanced outcome for both user types.

In particular, to assess the effectiveness of the proposed Optimized Phase Shifts and Power Control (OPS-OPC) design, it has been compared to a benchmark scheme called Random Phase Shifts and Equal Power Control (RPS-EPC). In this comparison, the transmit power is evenly distributed among all users, utilizing a random phase shift matrix at the RIS. Figure 7.3.6-2 shows the Cumulative Distribution Function (CDF) for the weighted minimum SE sum among NFUEs and FFUEs using CZF, LZF, and MRT precoding. There are 5 NFUEs and 5 FFUEs and the Space Division Multiple Access (SDMA) is adopted in considered scenario, i.e. all the users are served simultaneously in the spatial domain. The proposed OPS-OPC scheme significantly outperforms RPS-EPC across all precoding techniques. With CZF, OPS-OPC reaches a median SE of 6,2 bits/s/Hz, which is a 37 % increase over RPS-EPC's 4,5 bits/s/Hz. For LZF, the improvement is 41 %, and with MRT, the median SE rises by 133 % (from 2 bits/s/Hz, 4 bits/s/Hz to 5 bits/s/Hz, 6 bits/s/Hz). Notably, LZF performs similarly to CZF in both schemes, making it an efficient alternative due to its lower computational complexity, particularly for large arrays.

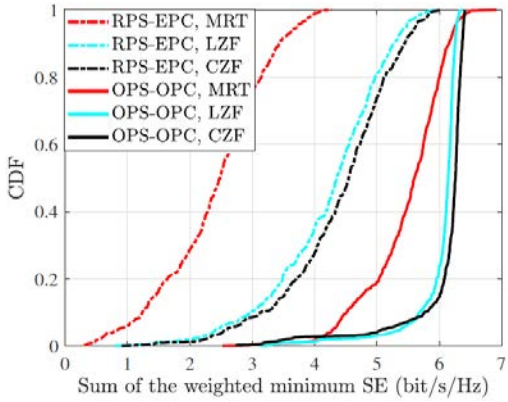

Figure 7.3.6-2: Comparison of Different Precoding Schemes

7.3.7 Beam Training Structure for Near-Field Cascaded Channels

For RIS assisted communications, characterizing the end-to-end channel is critical for effective beamforming. A conventional approach might involve estimating the individual BS-RIS and RIS-UE links separately, a process that is inefficient, especially in the near-field where four distinct physical parameters (two distances, two angles) would need to be resolved. This proposal introduces a more efficient framework by deriving an equivalent singlehop model for the near-field cascaded link. The introduction of near-field effects, driven by the deployment of extremely large-scale arrays (XL-MIMO), necessitates a departure from far-field models. Our objective is to demonstrate that the beam training process can be fundamentally simplified by directly targeting the cascaded channel properties, rather than the properties of the constituent hops.

System Model Formulation: by defining the foundational channel models. Based on near-field propagation theory and utilizing a second-order Taylor series approximation for the phase, the channel vector $h \in \mathbb{C}^{N\times 1}$ for a single-hop link to a Uniform Linear Array (ULA) with N elements can be modeled. The n-th element of the vector is given by:

$$h[n] \approx \rho e^{j\phi[n]} = \rho e^{jk\left(p_1(nd)^2 + p_2 nd\right)}$$

where ρ is the complex channel gain, $k = 2\pi/\lambda$ is the wavenumber, and d is the element spacing. The parameters $p_1 = -\frac{\cos^2\theta}{2r}$ (Wavefront Curvature) and $p_2 = \sin\theta$ (Wavefront Direction) characterize the channel's geometric properties. For a BS-RIS-UE link, the goal of the RIS is to co-phase the signals from the two hops. The total phase variation across the RIS aperture, which should be compensated, is the sum of the phase variations from the BS-RIS link ($\phi_i[n]$) and the RIS-UE link ($\phi_r[n]$).

Proposed Equivalent Model and Parameter Definition: an equivalent virtual channel can be defined, h_{vtl}, whose phase represents this total phase accumulation. The phase of the n-th element of this virtual channel is:

$$\begin{aligned}\phi_{vtl}[n] &= \phi_i[n] + \phi_r[n] \\ &= k\left(p_{1,i}(nd)^2 + p_{2,i}nd\right) + k\left(p_{1,r}(nd)^2 + p_{2,r}nd\right) \\ &= k\left[\left(p_{1,i} + p_{1,r}\right)(nd)^2 + \left(p_{2,i} + p_{2,r}\right)nd\right]\end{aligned}$$

Therefore, the virtual channel vector's n-th element can be expressed as:

$$h_{vtl}[n] \approx \rho_{cas} e^{jk[(p_{1,i}+p_{1,r})(nd)^2+(p_{2,i}+p_{2,r})nd]}$$

where ρ_{cas} is the equivalent cascaded complex gain. A critical observation is that its mathematical structure is perfectly isomorphic to the single-hop near-field channel model. This leads to the central conclusion: A two-hop near-field cascaded channel can be precisely represented by an equivalent virtual single-hop near-field channel with a new set of effective parameters. To complete this equivalence, two equivalent cascaded channel parameters can be defined. The Equivalent Direction Parameter (β_2) is defined as:

$$\beta_2 \triangleq p_{2,i} + p_{2,r} = \sin\theta_i + \sin\theta_r$$

Since $\sin\theta_i, \sin\theta_r \in [-1,1]$, the range for β_2 is $[-2,2]$, identical to the far-field case. The Equivalent Curvature Parameter (β_1) is defined as:

$$\beta_1 \triangleq p_{1,i} + p_{1,r} = -\left(\frac{\cos^2\theta_i}{2r_i} + \frac{\cos^2\theta_r}{2r_r}\right)$$

The range of β_1 depends on the near-field bounds of both links. Since both $p_{1,i}$ and $p_{1,r}$ are non-positive, β_1 is also non-positive. Let the physical aperture of the RIS be D and the lower bound of the near-field distance be the Fresnel distance $d_N \approx 0{,}62\sqrt{D^3/\lambda}$. The range for the equivalent curvature parameter is approximately $\beta_1 \in \left[-\left(\frac{\cos^2\theta_i}{2d_{N,i}} + \frac{\cos^2\theta_r}{2d_{N,r}}\right), 0\right]$.

Redefinition of the Beam Training Problem. The derivation of this equivalent model fundamentally redefines the problem of near-field beam training for RIS-assisted systems. A conventional approach might attempt to estimate the four underlying physical parameters $(r_i, \theta_i, r_r, \theta_r)$ of the two separate hops, which is a high-dimensional and complex task. However, our model proves that such a separate estimation is unnecessary. The core task of nearfield beam training is thus transformed from estimating four independent physical parameters of the individual hops to determining the two cascaded parameters of the equivalent end-to-end channel: the equivalent curvature β_1 and the equivalent direction β_2. This transformation reduces the dimensionality of the search space from four to two (or three for a UPA), significantly simplifying the problem. The beam training search space is therefore defined by the equivalent parameters:

- Search Dimension 1 (Curvature): $\beta_1 \in \left[-\left(\frac{\cos^2\theta_i}{2d_{N,i}} + \frac{\cos^2\theta_r}{2d_{N,r}}\right), 0\right]$
- Search Dimension 2 (Direction): $\beta_2 \in [-2,2]$

This conclusion provides clear guidance for future work. Any beam training or channel estimation algorithm designed to estimate (p_1, p_2) for a single-hop near-field link can, in principle, be directly applied to the cascaded channel scenario by simply adapting its search range to the intervals defined for β_1 and β_2.

7.3.8 Robust beamforming scheme for RIS-assisted wideband ISAC systems

Integrated Sensing And Communication (ISAC) is a promising technology to share the spectrum and hardware between sensing and communications, which effectively improves the resource utilization efficiency [i.24]. Recent advancements in ISAC research have focused on enhancing the performance of both sensing and communication tasks. For instance, various techniques have been proposed to jointly optimize the beamforming, and power allocation for both sensing and communication functionalities. These strategies often aim to maximize the communication capacity while simultaneously improving sensing accuracy, resolution, and coverage. However, the transmitted signals probably suffer from significant attenuation and weak diffraction capabilities, resulting in limited communication distances. Particularly, when there are obstacles between the transmitter and receiver, communications are severely hindered. To address this, the low-cost, low-power RISs can be utilized. By optimizing RIS reflection coefficients, a virtual Line-of-Sight (LoS) link can be established, thereby extending the transmission distance and coverage range.

To mitigate frequency-selective fading, wideband multi-carrier transmission schemes most notably Orthogonal Frequency Division Multiplexing (OFDM) are widely adopted. Nevertheless, the frequency independent characteristics inherent in RIS components induce beam squint distortion a detrimental effect where discrete subcarrier beams diverge into disparate spatial directions, consequently compromising the overall beamforming gain. Additionally, from sensing perspective, beam squint may be advantageous since it can realize the rapid sensing, which has been demonstrated by relevant studies exploring the application of beam squint in sensing. Based on the above analysis, it is evident that beam squint produces distinct effects for sensing and communication, highlighting the importance of a joint study on RIS beam squint effects in wideband ISAC.

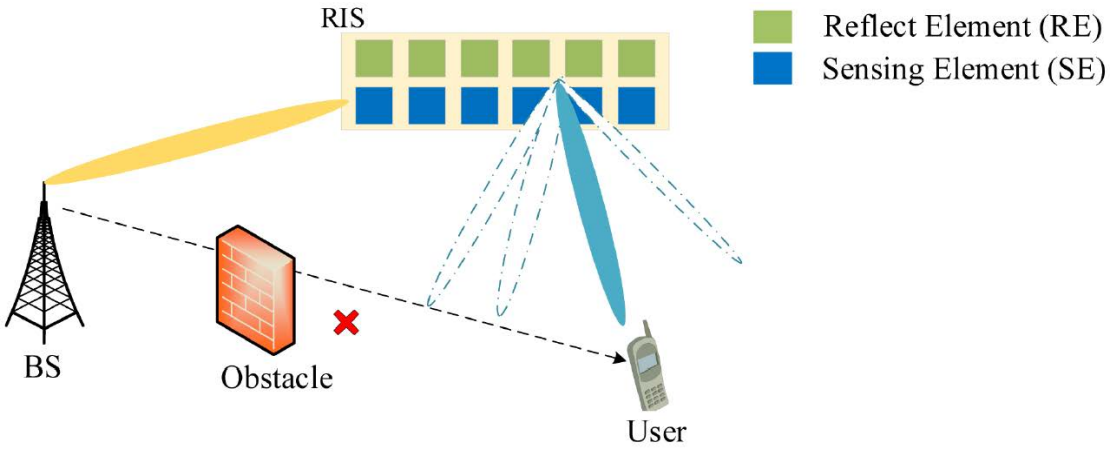

Figure 7.3.8-1: A RIS-assisted wideband ISAC system

As shown in Figure 7.3.8-1, a RIS-assisted wideband ISAC system has been investigated, which operates in two distinct stages: sensing and communication. To account for the beam squint effect, True Time Delay (TTD) units are integrated into RIS elements. Additionally, in order to mitigate transmission fading and enhance sensing capability, a subset of RIS elements is endowed with active sensing functionality, enabling the reception of echo signals.

In the sensing stage, a fast sensing scheme has been proposed that leverages the RIS beam squint effect by jointly configuring RIS reflection coefficients and corresponding time delays. Based on this, the Cramér-Rao Bound (CRB) for target user sensing has been derived, and analyse its dependence on the sensing angle and the Channel State Information (CSI) estimation error.

In the communication stage, a robust communication capacity maximization problem under imperfect CSI has been formulated, wherein RIS reflection coefficients, time delays, and sensing duration are jointly optimized. Due to the non-convex nature of the formulated problem, a two-step approach has been developed. First, the sensing duration is fixed. Then, an Alternating Optimization (AO) algorithm is developed to iteratively optimize RIS parameters. Specifically, by employing the S-procedure and Semi Definite Relaxation (SDR), each subproblem is transformed into a convex form and solved alternately. A one-dimensional search strategy is further applied to identify the optimal sensing duration.

Next, it presents a numerical example to validate the performance of the proposed scheme. The simulation parameters are configured as follows: the frame duration is set to 200 ms, the bandwidth is 6 GHz, and the carrier frequency is 300 GHz. The number of RIS-RE elements and RIS-SE elements are 32 and 16, respectively. Figure 7.3.8-2 illustrates the relationship between achievable capacity and SNR. As expected, as SNR increases, the capacity of all schemes increases. Additionally, for the same SNR, the proposed scheme consistently achieves the highest capacity compared to the baseline schemes, demonstrating the effectiveness of the proposed approach.

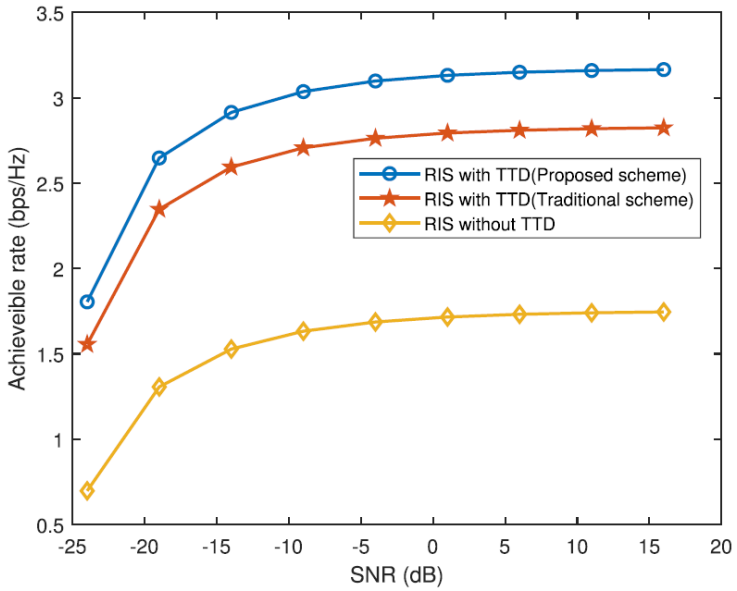

Figure 7.3.8-2: The achievable capacity versus the SNR

Details omitted in the above discussions can be referred to [i.28]. Besides, it is worth noting that, the above elaborations based on far-field propagation model can be extended to near-field scenarios straightforwardly, with only steering vectors different.

7.3.9 Other beamforming mechanisms

RIS technology enables sophisticated beam manipulation capabilities through precise control of phase across large arrays of reconfigurable elements. By leveraging the fine control and large aperture characteristics of RIS, it becomes possible to generate and manipulate various types of electromagnetic waves beyond conventional Gaussian beams, including Orbital Angular Momentum (OAM) beams [i.18], Airy beams, and Bessel beams, each offering unique propagation characteristics in near-field scenarios.

OAM beams can be considered as a space division multiplexing technique for achieving higher link capacity while maintaining the same bandwidth, and due to the inherent orthogonality between different OAM modes, each OAM mode can be seen as a separate data transmission channel independent of time, frequency, and polarization [i.29]. Airy beams exhibit self-healing properties and curved trajectory propagation, making them suitable for obstacle avoidance scenarios. Their asymmetric sidelobe distribution enables low-interference transmission while maintaining performance when partially obstructed. Bessel beams maintain their beam profile in the near-field up to specific distances with resistance to scattering effects. These non-diffracting properties provide stable power delivery compared to traditional beamforming techniques in near-field applications.

Dynamic reconfiguration of RIS elements allows real-time adaptation to match specific channel conditions, enabling enhanced beamforming precision and improved interference management tailored for near-field environments. Furthermore, beyond communication applications, these manipulated beams can be leveraged for RIS-assisted wireless sensing by exploiting their inherent physical properties, where the fundamentally different helical wavefront distribution of OAM beams, which does not share any commonalities with linearly or circularly polarized wavefronts, can allow RIS to perform communication and sensing tasks at the same frequency without interference. In this case, a Multi-Functional RIS (MF-RIS) with sensing capabilities [i.18] can be used as a wave transformer to convert the plane wave from BS into multiple OAM modes that contain ISAC frames. An example of such an MF-RIS architecture is considered in [i.22].

7.4 Codebook design mechanism

7.4.1 Near-Field RIS Codebook in Cartesian Coordinates

With the increasing number of RIS elements, the aperture size of RIS becomes larger and the Rayleigh distance increases accordingly. In this case, the scatters are more likely to be in the near-field region of RIS, and the near-field channel model should be considered. However, the existing far-field codebook mechanisms cannot be applicable to the near-field channel model, thus the new near-field codebook should be designed to match the near-field propagation characteristics.

According to the near-field channel model discussed in clause 6, it can be observed that the near-field cascaded channel is determined by the sum of the distance from the j-th transmit antenna to the RIS and the distance from the *i*-th receive antenna elements to the RIS, thus each codeword for the RIS should be related to a pair of sampled points in the coordinate system instead of only one sampled point [i.14].

In this way, it can be assumed that Ξ^{G_t} and Ξ^{r} represents the two collections of the sample point corresponding to $\left(x_{G_t}, y_{G_t}, z_{G_t}\right)$ and $\left(x_r, y_r, z_r\right)$ as described in clause 6.3. In this way, Ξ^{G_t} and Ξ^{r} can be represented as following [i.15]:

$$\begin{aligned}
&\Xi^{G_t} = \left\{\left(x_s^{G_t}, y_s^{G_t}, z_s^{G_t}\right)\right\},\\
&x_s^{G_t} = X_{\min}^{G_t}, X_{\min}^{G_t} + \Delta x^{G_t}, X_{\max}^{G_t};\\
&y_s^{G_t} = Y_{\min}^{G_t}, Y_{\min}^{G_t} + \Delta y^{G_t}, Y_{\max}^{G_t};\\
&z_s^{G_t} = Z_{\min}^{G_t}, Z_{\min}^{G_t} + \Delta z^{G_t}, Z_{\max}^{G_t};\\
&\Xi^{r} = \left\{\left(x_s^{r}, y_s^{r}, z_s^{r}\right)\right\},\\
&x_s^{r} = X_{\min}^{r}, X_{\min}^{r} + \Delta x^{r}, X_{\max}^{r};\\
&y_s^{r} = Y_{\min}^{r}, Y_{\min}^{r} + \Delta y^{r}, Y_{\max}^{r};\\
&z_s^{r} = Z_{\min}^{r}, Z_{\min}^{r} + \Delta z^{r}, Z_{\max}^{r};
\end{aligned}$$

where $\Delta x^{G_t}, \Delta y^{G_t}, \Delta z^{G_t}$ represents the sampling step on the x-y-z coordinates for Ξ^{G_t} respectively, $\Delta x^{r}, \Delta y^{r}, \Delta z^{r}$ represents the sampling step on the x-y-z coordinates for Ξ^{r} respectively. In such case, the sampled distance can be represented as following:

$$D_s(n_1, n_2) = \sqrt{\left(x_s^{G_t} - x_{n_1}\right)^2 + y_s^{G_t^2} + \left(z_s^{G_t} - z_{n_1}\right)^2} + \sqrt{\left(x_s^{r} - x_{n_1}\right)^2 + y_s^{r^2} + \left(z_s^{r} - z_{n_1}\right)^2}$$

According to above equation and the channel model described in clause 6.3, it can be clearly observed that the near-field codeword can be designed and represented by such cascaded array steering vector as following:

$$c_s = \left[e^{-j2\pi D_s(1,1)}, \cdots, e^{-j2\pi D_s(1,N_2)}, \cdots, e^{-j2\pi D_s(N_1,1)}, \cdots, e^{-j2\pi D_s(N_1,N_2)}\right]$$

which can be used to represent as a column in the near-field codebook W to reflect a beamforming vector θ at the RIS. By calculating all distance of each sample points and combined it as a whole matrix, the near-field codebook set can be obtained. The users can search the whole codebook set to find the optimal codeword.

In this way, it can be observed that the size of codebook set is highly related to the number of sampling points in Ξ^{G_t} and Ξ^{r} when the sampling step is small, it means the codebook subset includes a large number of codewords, which increases the complexity of beam training. While when increasing the value of sampling step, the number of codewords included in the codebook set will be decreased, however, the accuracy of beam training will also be impacted, which may have the negative impact of the transmission performance. Thus, when determining the sampling step, the trade-off between the complexity and the performance gain should be considered.

7.4.2 Near-Field Codebook Design for THz RIS-Aided Systems

In an RIS-aided system, the signal traverses a two-hop BS-RIS-UE link in a cascaded channel. The phase of the signal arriving at the UE from a point x_n on the RIS aperture is affected by the quadratic phase terms from both the incident (BS-RIS) and reflected (RIS-UE) paths. While the RIS compensates for the linear phase terms to achieve beamforming, the quadratic terms remain. The total residual phase error, $\Delta\Phi_{\text{total}}(x_n)$, is the sum of the errors from each hop:

$$\Delta\Phi_{\text{total}}(x_n) = -\frac{2\pi}{\lambda}\left(\frac{x_n^2\cos^2\theta_i}{\|2\mathbf{r}_{\text{BS-RIS}}\|} + \frac{x_n^2\cos^2\theta_r}{\|2\mathbf{r}_{\text{RIS-UE}}\|}\right)$$

where $\mathbf{r}_{\text{BS-RIS}}$ and $\mathbf{r}_{\text{RIS-UE}}$ are the 3D distance vectors between the BS-RIS and RIS-UE respectively, θ_i and θ_r are the incidence and reflection angles (in degrees) on the RIS, λ is the wavelength, D is the effective aperture diameter of the RIS, and $\|\cdot\|$ is the Euclidean norm. The maximum total phase error across the aperture D is therefore additive:

$$\Delta\Phi_{\text{total, max}} = \frac{\pi D^2}{4\lambda}\left(\frac{\cos^2\theta_i}{\|\mathbf{r}_{\text{BS-RIS}}\|} + \frac{\cos^2\theta_r}{\|\mathbf{r}_{\text{RIS-UE}}\|}\right)$$

When this equation is extended to the element level, incorporating the quadratic phase of each RIS unit cell, it becomes:

$$\Delta\Phi_{\text{total, max}}(m,n) = \frac{\pi}{\lambda}\left(x_{m,n}^2 + y_{m,n}^2\right)\left(\frac{\cos^2\theta_i}{\|\boldsymbol{r}_{m,n}^{\text{BS-RIS}}\|} + \frac{\cos^2\theta_r}{\|\boldsymbol{r}_{m,n}^{\text{RIS-UE}}\|}\right)$$

This per-element form explicitly represents the quadratic curvature across the RIS aperture. Elements located further from the RIS center experience larger quadratic phase shifts, resulting in beam spread or defocusing if uncorrected. Therefore, when the transmitter or receiver lies within the near-field region $< 2D^2/\lambda$ i.e. the Fraunhofer distance of the RIS, the impinging and reflected wavefronts should be modeled as spherical rather than plane waves to maximize the RIS beamsteering gain [i.26]. This relationship is modeled through the Green's function-based 3D electric field coupling between the BS, the RIS unit cell elements *(m,n)*, and the UE:

$$\boldsymbol{E}(\boldsymbol{r}) = \sum_{m=1}^{M}\sum_{n=1}^{N}\Gamma_{m,n}\frac{e^{-jk\left(\|\boldsymbol{r}_{m,n}^{\text{BS-RIS}}\| + \|\boldsymbol{r}_{m,n}^{\text{RIS-UE}}\|\right)}}{\|\boldsymbol{r}_{m,n}^{\text{BS-RIS}}\|\cdot\|\boldsymbol{r}_{m,n}^{\text{RIS-UE}}\|}, k = \frac{2\pi}{\lambda}$$

where $\Gamma_{m,n}$ is the reflection (or scattering) coefficient of the *(m,n)*'th RIS unit cell element, $\boldsymbol{r}_{m,n}^{\text{BS-RIS}}$ is the 3D distance vector between the transmitter BS and the *(m,n)*'th RIS unit cell element, and $\boldsymbol{r}_{m,n}^{\text{RIS-UE}}$ is the respective 3D distance vector to the receiver UE.

By appropriately adjusting $\Gamma_{m,n}$, the superposition of the scattered fields from all unit cells can be engineered to focus the beam within the near-field region. Then, by choosing the unit cell phase shifts $\Psi_{m,n}$, the RIS can be programmed to focus the reflected wave on the target. The fundamental requirement for beam focusing is to ensure that all unit cell element contributions add up in-phase at the focal point. In other words, the phase delays due to propagation from BS to *(m,n)* and from *(m,n)* to UE should be exactly compensated by the RIS unit cell element's added phase and the RIS focal point. To achieve that, the RIS near-field codebook is constructed by considering the time reverse of the optimal waves (the backward propagation of the optimal waves), as per [i.27], and compensating for the quadratic phase error accumulation in the cascaded channel:

$$\Psi_{m,n} = mod\left\{-k\left(\|\boldsymbol{r}_{m,n}^{\text{BS-RIS}}\| + \|\boldsymbol{r}_{m,n}^{\text{RIS-UE}}\|\right) - \frac{k}{2}\left(x_{m,n}^2 + y_{m,n}^2\right)\left(\frac{\cos^2\theta_i}{\|\mathbf{r}_{\text{BS-RIS}}\|} + \frac{\cos^2\theta_r}{\|\mathbf{r}_{\text{RIS-UE}}\|}\right), 2\pi\right\}$$

Therefore, each codebook entry corresponds to the conjugate phase profile of the desired focal field distribution, compensating both the propagation delay and residual quadratic phase error in the cascaded channel. The illustration of the beam pattern is provided in Figure 7.4.2-1, including the measurement comparison with and without the RIS.

To quantify the expansion of the near-field range in cascaded channels, a simulation was conducted using a 0,8 m by 0,8 m aperture at 3,5 GHz, corresponding to a conventional Rayleigh distance of approximately 30 m. Figure 7.4.2-2 compares the spatial power loss of far-field beamforming relative to ideal near-field focusing. Two setups are evaluated: a direct BS link and an RIS-aided link where the BS is positioned at 35 m to ensure the incident link is strictly within the far-field region. The white dashed contour indicates the valid far-field zone where the phase error remains below the standard threshold of pi/8.

The results indicate a significant disparity. For the direct BS link, the valid far-field zone begins immediately beyond the Rayleigh distance of 30 m. In contrast, for the RIS cascaded link, no valid far-field zone appears even at distances extending up to 400 m. This confirms that the accumulation of wavefront curvature from both the incident and reflected paths renders the conventional far-field approximation invalid for RIS systems, even at distances significantly exceeding the traditional Rayleigh limit. Although the simulations in this contribution were performed at 3,5 GHz to illustrate the fundamental physics of cascaded channels, these findings are even more critical for TeraHertz (THz) scenarios. In THz bands, the extremely short wavelengths inherently create large Rayleigh distances. Consequently, the significant expansion of the near-field boundary caused by the accumulation of residual quadratic phase errors makes this near-field codebook design essential for efficient THz RIS implementation.

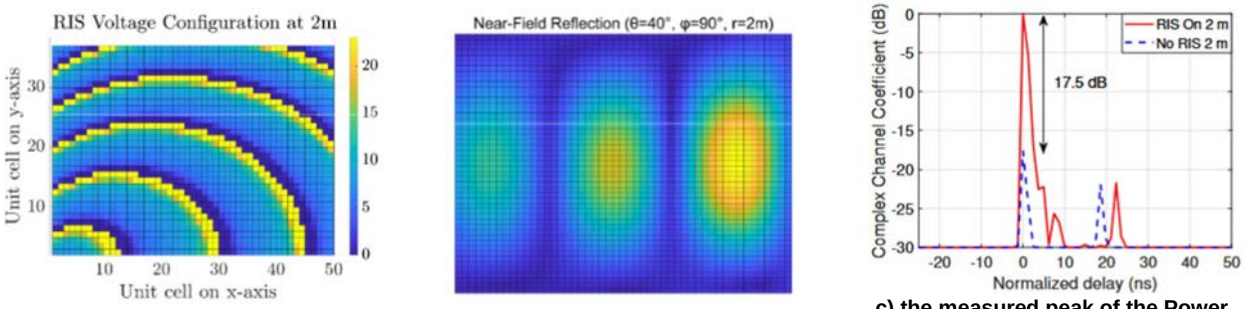

a) varactor diode voltage

b) simulated reflection beam pattern

c) the measured peak of the Power Delay Profile (PDP) in the near-field for both RIS on and no-RIS cases

Figure 7.4.2-1: 50 × 37 RIS near-field phase synthesis at 3,5 GHz for the reflection angle θ_r= 40°, ϕ_r= 90°, and r_{RIS-UE} = 2 m

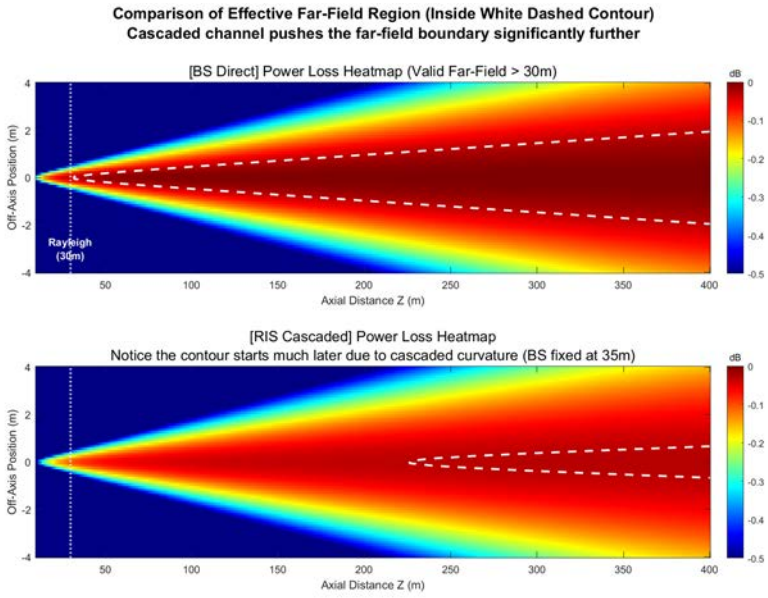

NOTE: The results demonstrate that the RIS cascaded channel may significantly expand the near-field boundary beyond the conventional Rayleigh distance due to the accumulation of residual quadratic phase errors from both the incident and reflected paths.

Figure 7.4.2-2: Comparison of the effective far-field region (indicated by the white dashed contour) between a direct BS link and an RIS cascaded link

7.5 Other mechanisms

7.5.1 Deployment Solutions

From a network operator's perspective, optimizing RIS deployment is essential to achieve cost-effective and high-performance networks. Key considerations include RIS placement, size, architecture/type, densities, orientations, and reflection configurations. For instance, strategic RIS positioning can significantly enhance signal strength and coverage, especially in connectivity-challenged areas. Besides, properly deployed distributed RISs are able to create rich-scattering environments, enabling multi-stream transmissions across the network and significantly boosting communication rates. Moreover, by employing multi-hop transmission with optimized reflective routing paths, robust Line-of-Sight (LoS) links can be established to blind spots to guarantee seamless coverage.

However, several critical challenges persist in the deployment and networking of RISs. First, the optimization of RIS deployment should be jointly coordinated with time, frequency, and spatial resource allocation to maximize overall network performance. For instance, different RIS deployment strategies may necessitate distinct multi-user access schemes, potentially leading to significant performance variations. Second, the coexistence of heterogeneous network nodes - including multiple Base Stations (BSs), passive and active RISs, and distributed user devices - coupled with diverse network topologies and complex node associations, poses substantial challenges for joint coordination and optimization. In particular, the mechanisms for achieving low-cost and energy-efficient networking with multiple RISs remain underexplored and unclear. Finally, practical considerations such as power consumption, energy supply, environmental conditions, and maintenance requirements should be taken into account in deploying RISs in commercial networks. These factors further compound the deployment of RISs. Addressing these challenges is paramount to unlocking the full potential of RIS technology, enabling better network performance, broader coverage, and cost-effective services.

RIS deployment for multi-point scenarios with multiple users/clusters distributed far apart is examined. Given a fixed number of RIS elements, two common deployment architectures are considered to minimize the two-hop path-loss: centralized RIS and distributed RIS, as illustrated in Figure 7.5-1. In the centralized architecture, all RIS elements are co-located near the BS. In contrast, the distributed architecture partitions all RIS elements into smaller RIS units, each deployed near a user cluster. The following discusses these two architectures for both single-antenna and multi-antenna cases.

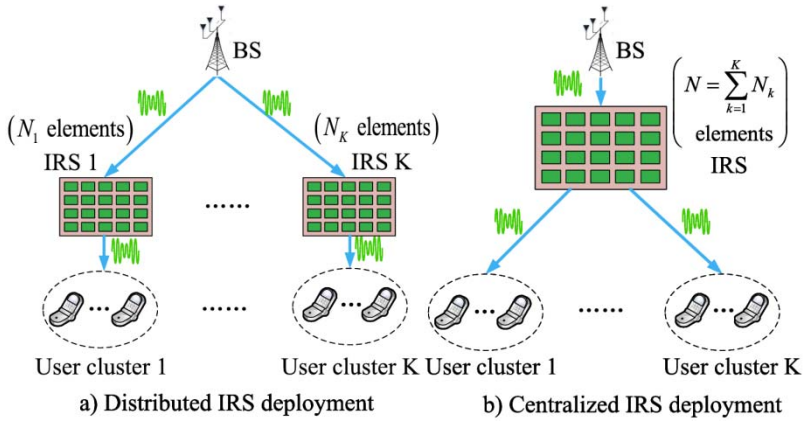

Figure 7.5-1: RIS-aided multi-user communication system with different RIS deployment strategies

In the single-antenna case, the effective channels from the BS to the K users are reduced to K scalars, making the capacity/achievable region of the RIS-aided multi-user system highly dependent on the corresponding channel power gains. It can be proven that a centralized RIS outperforms a distributed RIS in terms of the capacity region. This is because co-located RIS elements in a centralized architecture provide higher Degree of Freedom (DoF) to balance users' individual channel gains, while small distributed RIS units primarily enhance users within their local coverage. However, this advantage applies only to passive RISs. For active RISs, deployment should further account for amplification ability. Centrally deploying an active RIS near the BS significantly limits its amplification capability, suggesting that the optimal deployment architecture for active RISs remains unclear and warrants further investigation.

Equipping the BS with multiple antennas enables efficient spatial domain exploitation to serve multiple users simultaneously. Consequently, RIS deployment should account for both user channel power gains and spatial multiplexing gains, differing fundamentally from the single-antenna case. A recent work [i.17] developed a theoretical framework to compare the system capacity of centralized RIS and distributed RIS deployment architecture under the homogeneous channel setup. By capturing their distinct channel characteristics, the study first identifies the capacity-achieving scheme for each architecture, which lays the foundation for performance comparison. For distributed RISs, an ideal deployment condition can create orthogonal channels, allowing spatial division multiple access as the optimal scheme. In contrast, for centralized RISs, highly correlated user channels which are common in LoS-dominated BS-RIS links necessitate a Time Division Multiple Access (TDMA)-based capacity-achieving scheme. Here, dynamic RIS beamforming maximizes each user's channel gain during alternating transmissions.

To compare the capacity of the two RIS deployment architectures in a multi-antenna network, a numerical example for an RIS-aided broadcast channel is illustrated in [i.17], showing the sum-rates versus the total number of RIS elements N. It is observed that the centralized RIS outperforms the distributed RIS when N is small. In this low-N region, system capacity is dominated by user-received power, and the centralized RIS benefits from a larger passive beamforming gain, significantly enhancing received power. However, as N exceeds a threshold, the distributed RIS achieves higher sum-rates, with the performance gap widening as N increases. This is because, in the large-N region, the spatial multiplexing gain of distributed RIS is fully exploited. Hence, for practical systems with large N, the distributed RIS architecture is preferable for boosting the capacity of multi-antenna networks.

It should be emphasized that, although the above elaborations are based on far-field propagation model, they also hold for near-field counterpart. The reason lies in that, regardless of far-field or near-field channel characteristics, when N is small, the centralized RIS achieves a significantly large passive beamforming gain since the user-received power dominates the system capacity, while for large-N region, distributed RIS realizes a remarkably high spatial multiplexing gain by constructing orthogonal/near-orthogonal channels with appropriate RIS deployment.

A significant difference between far-field and near-field propagation environment lies in BS-RIS channel. For far-field scenario, the BS-RIS channel exhibits significant rank deficiency, especially for high frequency communications where NLOS paths are rarely available. In contrast, high-rank channel property becomes much more apparent when the devices fall in near-field region. Hence, the centralized RIS may achieve a larger spatial multiplexing gain compared to far-field case. However, passive RISs are preferred to be deployed much closer to the users for providing remarkable passive beamforming gain. This fact implies that, although the BS-RIS channel is modelled as near-field channel, it is still rank deficient, which is indeed similar to the far-field counterpart. Hence, the aforementioned RIS deployment solutions are generic, which is suitable for not only far-field but also near-field scenarios.

7.5.2 Near-Field RIS Placement Scheme Design

Near-field RIS deployment presents a promising avenue for enhancing channel rank and enabling multi-stream transmission, contrasting with the rank limitations inherent in far-field planar wave approximations under LoS conditions. The spherical wavefronts characteristic of the near-field regime induce significant spatial variations in phase and amplitude across RIS elements, thereby substantially increasing the rank of the channel matrix. This is particularly relevant for emerging wireless systems featuring large apertures or short communication distances. This inherent spatial diversity allows the system to serve multiple single-antenna users with independent data streams simultaneously, directly contributing to an increased channel rank. Consequently, the enhanced rank achieved through near-field RIS deployment directly supports high-capacity multi-stream transmission in MIMO systems, establishing it as a critical technology for future high-performance wireless communication paradigms.

As shown in Figure 7.5.2-1, it considers a multi-user MIMO communication system through a RIS, with a BS and K UEs, where uniform arrays are equipped at both the BS and RIS with N_{BS} antennas and N_{RIS} elements, repectively. It is assumed that the ULA at the BS is placed along the y-axis and centered at the origin. Therefore, the location of the m-th array element of the BS is given by $\mathrm{w_m} = [0, \mathrm{md_{BS}}]^{\mathrm{T}}$,where $m \in \{0, \pm1, \ldots, \pm(\mathrm{N_{BS}} - 1)/2\}$ and $\mathrm{d_{BS}} = \lambda/2$ with λ denoting the wavelength. The center of the ULA corresponding to the RIS is denoted as $p = [-l\cos\varphi, l\sin\varphi]^{\mathrm{T}}$, where l is the distance between the array center of RIS and the origin, and $\varphi \in [-\pi/2, \pi/2]$ denotes the direction of the central element at RIS with respect to the BS's boresight. Therefore, for the RIS, the location of its n-th element can be expressed as $\mathrm{p_n} = p + \delta_{\mathrm{n}}$with $n \in \{0, \pm1, \ldots, \pm(\mathrm{N_{RIS}} - 1)/2\}$, and δ_{n} denotes the location of the n-th element relative to the reference point p. Let $\theta \in [-\pi/2, \pi/2]$ denote the angle between p and the normal vector of the ULA at the RIS, and δ_{n} can be expressed as $\delta_{\mathrm{n}} = [-\mathrm{nd_{RIS}}\sin(\theta - \varphi), \mathrm{nd_{RIS}}\cos(\theta - \varphi)]^{\mathrm{T}}$, where $\mathrm{d_{RIS}} = \lambda/2$.

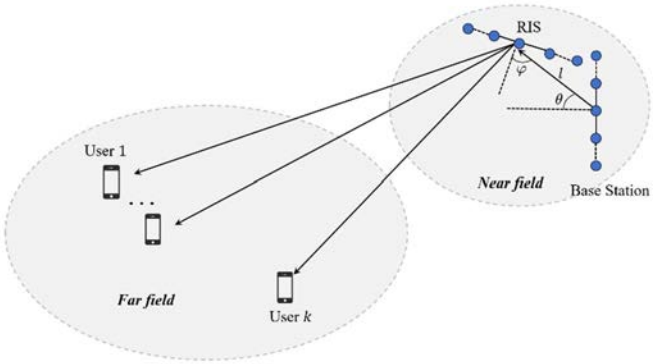

Figure 7.5.2-1: Multi-user MIMO communication system through a RIS

For the k-th user, the channel $\mathrm{h_k} \in \mathrm{C}^{\mathrm{N_{BS}}\times 1}$ from the BS to the user through the RIS can be denoted as:

$$h_k = F\Phi t_k = [h_k(1), h_k(2)\cdots, h_k(N_{BS})]^T,$$

where $F \in C^{N_{BS}\times N_{RIS}}$ and $t_k \in C^{N_{IRS}\times 1}$ denote the channel from the BS to the RIS and the RIS to the k-th user, repectively, $\Phi \in \mathrm{C}^{\mathrm{N_{RIS}}\times \mathrm{N_{RIS}}}$ denotes the RIS phase shift matrix, $h_k(m) = \beta_k \sum_{n=-L}^{L} e^{j\phi_n} e^{-j\frac{2\pi}{\lambda}(l_{m,n}+d_{n,k})}$ with β_k and ϕ_n denoting the reference complex-valued channel gain and the phase of the n-th element on the RIS, $l_{m,n}$ and $d_{n,k}$ denote the distance from the m-th antenna of the BS to the n-th element of the RIS, $L = \frac{N_{IRS}-1}{2}$, and the distance from the n-th element of the RIS to the k-th user, respectively. Next, it focus on the correlation study of two users.

The correlation between the i-th user and the j-th user is defined as:

$$\rho_{ij} = \frac{|h_i^H h_j|^2}{||h_i||^2 ||h_j||^2}.$$

When the RIS is in the far-field of the BS, and all users are also in the far-field of the RIS, $\rho_{ij}^{far} = 1$.

In this scenario, the BS-to-RIS channel $\boldsymbol{F}$ has rank one because of the far field direct path. This causes the effective channels for different users to be perfectly correlated (correlation coefficient = 1). As a result, the system's spatial multiplexing gain is significantly reduced and cannot be improved by adjusting the RIS phases. For this reason,the RIS has been placed in the near-field of the BS, which makes the BS-to-RIS channel exhibit higher rank, thereby enabling the reduction of interference for multiple single-antenna users.

When the RIS is in the near-field of the BS, and all users are in the far-field of the RIS, to evaluate the decorrelation between two user channels, a metric under randomly configured RIS phases have been investigated. It considers the propagation conditions to be favourable when this variance approaches zero as follows:

$$g_{i,j} \triangleq \mathrm{var}\left\{\frac{\overline{h_i^H}\overline{h_j}}{\sqrt{E\left\{||\overline{h_i}||^2\right\}E\left\{||\overline{h_j}||^2\right\}}}\right\} \to 0,$$

After a series of derivations:

$$g_{i,j} \approx \frac{1}{(N_{IRS}N_{BS})^2}\sum_{n,s,n\neq s}\left(\frac{\sin\left(N_{BS}\frac{\lambda\pi(n-s)\cos\varphi\cos\theta}{4l}\right)}{\sin\left(\frac{\lambda\pi(n-s)\cos\varphi\cos\theta}{4l}\right)}\right)^2,$$

where λ is wavelength. Obviously, it cannot make $g_{i,j}$ equal to 0.

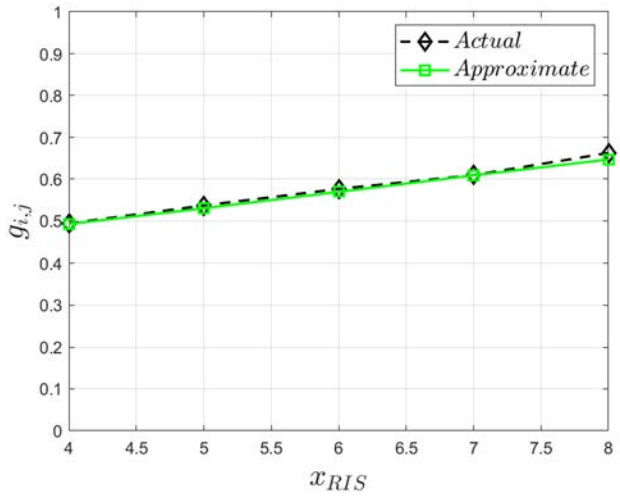

Figure 7.5.2-2: $g_{i,j}$ versus RIS location

In Figure 7.5.2-2, it compares the actual $g_{i,j}$ values with those obtained from our closed-form formula for various RIS positions. The locations of the BS and the RIS are set at (0, 0) and (x_{RIS}m, 5 m), respectively. The simulation results show that our formula accurately describes the actual $g_{i,j}$. Thus, by deploying the RIS according to $\cos\varphi\cos\theta = \frac{4l}{N_{BS}\lambda}$, it can make $g_{i,j}$ take on a smaller value, thereby increasing the channel rank of the BS-to-RIS link and reducing the correlation between user channels.

7.5.3 Dual-IRS Aided Near-/Hybrid-Field Wireless Information and Power Transmission in THz Networks

Intelligent Reflecting Surface (IRS) is a promising technology for TeraHertz (THz) SWIPT systems. It has the capability to establish additional transmission links and reconfigure the wireless propagation environment. Since THz signals suffer from severe path loss and are highly sensitive to blockage, the reflective link enabled by IRS is crucial. It substantially enhances the received signal power and coverage when the direct link is obstructed. Deploying the IRS in proximity to the BS can make the BS-IRS channel exhibit a higher rank, thereby enabling interference mitigation. However, due to the extremely short wavelength in THz bands, the radiative near-field region expands significantly. Consequently, the BS and IRS are likely to fall into each other's near-field region even at practical deployment distances. In this scenario, the far-field plane-wave assumption no longer holds, and spherical-wave propagation should be considered. Moreover, taking user mobility into account, the system may operate under a hybrid-field model. For instance, the BS-IRS link lies in the near field while the IRS-user link remains in the far field. This makes channel modelling more intricate and poses significant challenges to system optimization.

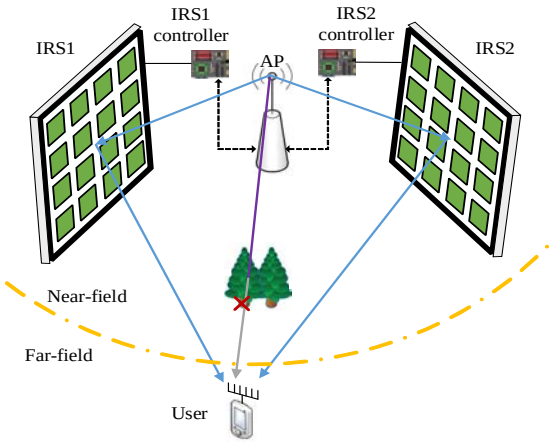

Figure 7.5.3-1: The near-field dual-IRS aided SIMO SWIPT system

As shown in Figure 7.5.3-1, it considers a dual-IRS-aided SWIPT system, where a single-antenna AP adjacent to two auxiliary IRSs serves a multi-antenna user, suffering a dominant interference from IN. The user is equipped with an M-element Uniform Linear Array (ULA), while the IN employs a single antenna. Each user antenna adopts an independent Power-Splitting (PS) scheme, allocating ρ_m ($0 \le \rho_m \le 1$) of the received signal power to Information Fecoding (ID) and $1-\rho_m$ to Energy Harvesting (EH). Two IRSs, denoted by IRS1 and IRS2, are modeled as Uniform Planar Arrays (UPAs) placed on the x-z plane. Specifically, IRS1 and IRS2 consist of $N_a = N_{x_a} \times N_{z_a}$ and $N_b = N_{x_b} \times N_{z_b}$ reflecting elements, respectively, and the element spacing along the x- and z-axis is ε. Each reflecting element has a physical size of $\sqrt{A} \times \sqrt{A}$ with $\sqrt{A} \le \varepsilon$. It assume that the AP antenna is placed at the origin of the three-dimensional (3D) Cartesian coordinate system, i.e. $\mathrm{p}_\mathrm{A} = (0,0,0)$. Denote the central locations of the (n_x, n_z)-th element of IRS1 and IRS2 as $\mathrm{p}_{n_{x_a},n_{z_a}} = \left[l_{x_a} + n_{x_a}\varepsilon, l_{y_a}, n_{z_a}\varepsilon\right]$ and $\mathrm{p}_{n_{x_b},n_{z_b}} = \left[l_{x_b} + n_{x_b}\varepsilon, l_{y_b}, n_{z_b}\varepsilon\right]$, respectively.

For the near-field BS-IRS1 channel, the channel power gain between the AP antenna and the $\left(n_{x_a}, n_{z_a}\right)$-th element of IRS1 can be derived as:

$$q_{n_{x_a},n_{z_a}} = \frac{1}{4\pi\left\|\mathrm{p}_\mathrm{A} - \mathrm{p}_{n_{x_a},n_{z_a}}\right\|_2^2} A \frac{\left(\mathrm{p}_\mathrm{A} - \mathrm{p}_{n_{x_a},n_{z_a}}\right)^T \mathbf{u}_a}{\left\|\mathrm{p}_\mathrm{A} - \mathrm{p}_{n_{x_a},n_{z_a}}\right\|_2} = \frac{A l_{y_a}}{4\pi l_{x_a}^3 \left[1 + \bar{r}_a^2 + 2n_{x_a}\xi_a + \left(n_{x_a}^2 + n_{z_a}^2\right)\xi_a^2\right]^{\frac{3}{2}}},$$

Accordingly, the channel response vector of the IRS1-user link, denoted by $\mathbf{h}_a \in \mathbb{C}^{N_a \times 1}$, is given by:

$$h_{n_{x_a},n_{z_a}} = \sqrt{q_{n_{x_a},n_{z_a}}}\, e^{-j\frac{2\pi}{\lambda_0} r_{n_{x_a},n_{z_a}}}, \forall n_{x_a}, n_{z_a},$$

Where $r_{n_{x_a},n_{z_a}} = \left\|\mathrm{p}_\mathrm{A} - \mathrm{p}_{n_{x_a},n_{z_a}}\right\|_2$.

The channel vector of BS-IRS1 link is established similar as IRS1. The far-field IRS1/IRS2-user channels $\mathbf{G}_a$ and $\mathbf{G}_b$, are assumed to follow the Rician fading channel model (or a sparse multipath model), accounting for the limited scattering characteristics typically observed in THz propagation.

Define $\mathbf{g}_a = \mathbf{G}_a \boldsymbol{\Theta}_a \mathbf{h}_a$ and $\mathbf{g}_b = \mathbf{G}_b \boldsymbol{\Theta}_b \mathbf{h}_b$ as the combined channels via IRS1 and IRS2, respectively. By the Lindeberg-Lévy central limit theorem, $\mathbf{g}_a \sim \mathrm{CN}\left(0, \tilde{\mathrm{n}}_a^2 \mathbf{I}\right)$ and $\mathbf{g}_b \sim \mathrm{CN}\left(0, \tilde{\mathrm{n}}_b^2 \mathbf{I}\right)$ can be obtained, with the average combined channel gain of the AP-IRS1-user link given by:

$$\tilde{\mathrm{n}}_a^2 = \frac{\beta A l_{y_a}}{4\pi l_{x_a}^3 d_a^\alpha} \sum_{n_{x_a}=-\frac{N_{x_a}-1}{2}}^{\frac{N_{x_a}-1}{2}} \sum_{n_{z_a}=-\frac{N_{z_a}-1}{2}}^{\frac{N_{z_a}-1}{2}} \frac{1}{\left(1 + \bar{r}_a^2 + 2n_{x_a}\xi_a + \left(n_{x_a}^2 + n_{z_a}^2\right)\xi_a^2\right)^{\frac{3}{2}}},$$

where $\bar{r}_a = l_{y_a} / l_{x_a}$, $\xi_a = \varepsilon / l_{x_a}$, α accounts for the pass loss exponent between the user and dual-IRS, β represents the reference path gain at a distance of 1 meter, and d_a stands for the distance between the user and IRS1. The combined channel gain of the AP-IRS2-user link is similar as $\tilde{\mathrm{n}}_a^2$. It can be observed that the combined channel gains are independent of the beamforming vectors of the two IRSs, yet they scale with the number of reflecting elements. Therefore, the optimization of a dual-IRS-aided SWIPT system under the hybrid-field model can be simplified into a tractable problem.

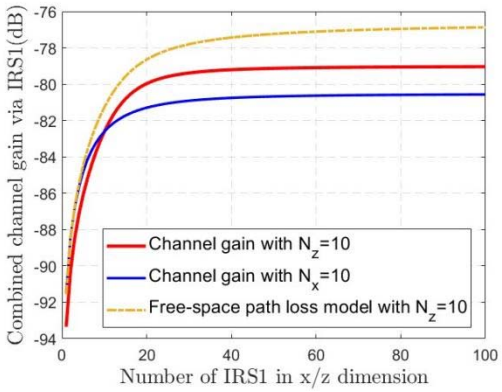

Figure 7.5.3-2: $\tilde{n}_a^2$ versus the number of IRS1 elements in x or z dimension

In Figure 7.5.3-2, it shows the combined channel gain $\tilde{n}_a^2$ for the AP-IRS1-user link versus the number of IRS1 elements along the x- or z-axis. For the sake of comparison, it considers the free-space path loss model for the AP-IRS1 channel, which does not account for the projected aperture. With N_z fixed at 10 and $N_x > 40$, or with N_x fixed at 10 and $N_z > 40$, the channel gain saturates at a constant value, whereas the free-space path loss model continues to increase, indicating its overestimation of the combined channel gain due to the omission of the projected aperture.

8 Conclusion and Recommendations

Near-field effects are critical to fully characterize RIS-aided communication networks. Further studies regarding the standard impact are encouraged.

History

Version	Date	Status
V1.1.1	February 2026	Publication